NASA TM X-706

TECHNICAL MEMORANDUM

X-706

TRANSONIC AERODYNAMIC CHARACTERISTICS OF THREE V/STOL FIGHTER MODELS WITH VARIABLE-SWEEP OR SKEWED WINGS AND DIFFERENT ENGINE INSTALLATIONS

By Francis J. Capone and Edwin E. Lee, Jr.

Langley Research Center
Langley Station, Hampton, Va.

NATIONAL AERONAUTICS AND SPACE ADMINISTRATION

WASHINGTON

September 1962

NATIONAL AERONAUTICS AND SPACE ADMINISTRATION

TECHNICAL MEMORANDUM X-706

TRANSONIC AERODYNAMIC CHARACTERISTICS OF THREE V/STOL FIGHTER MODELS WITH VARIABLE-SWEEP OR SKEWED WINGS AND DIFFERENT ENGINE INSTALLATIONS*

By Francis J. Capone and Edwin E. Lee, Jr.

SUMMARY

An investigation has been conducted in the Langley 16-foot transonic tunnel to determine the aerodynamic characteristics of three twin-jet variable-sweep fighter configurations having multimission capabilities. Tests were conducted at Mach numbers from 0.70 to 1.08 and angles of attack from -2° to 7°. The Reynolds number per foot varied from 3.57×10^6 to 4.35×10^6. Two of the models had identical variable-sweep wings with the outboard panels swept 80°, and the third had a straight wing skewed 90° about a central pivot. One of the variable-sweep models had nacelles suspended from the fuselage afterbody, and on the other two configurations the jet exits were located in the fuselage base.

The results of the investigation indicate that all models were longitudinally stable and exhibited low lift-curve slopes. The critical Mach number for all configurations was approximately 0.90 and the drag-rise increments ranged from 50 to 70 percent of the subsonic drag level. The configuration with nacelles produced the lowest drag rise but had the highest overall drag coefficient level.

INTRODUCTION

The National Aeronautics and Space Administration is conducting an extensive research program to evaluate the multimission performance capabilities of various tactical fighter configurations incorporating variable-wing-sweep techniques. The desired operating characteristics include short-field take-offs and landings, long-range subsonic flight for ferry and loiter operations, and supersonic operation at both sea level and altitude. Transonic and supersonic aerodynamic data are given

in references 1 to 8 for some of the configurations already tested in this program.

The present investigation was conducted to determine the relative aerodynamic characteristics of three fighter configurations having different types of variable-geometry wings and engine installations. Minimum drag characteristics under conditions approximating the low-level attack mission were of particular interest. Two of these configurations used identical outboard-pivot type variable-sweep wings with the leading edges of the outer panels swept 80°. The third configuration involved a "skewed wing" positioned with the 50-percent-chord line in the streamwise direction. Results for another configuration employing this particular wing concept are given in references 9 and 10. One of the variable-sweep models had strut-mounted engine nacelles located on the fuselage afterbody and the other two configurations had two-dimensional side inlets ducted to twin jet exits in the fuselage base to represent aircraft with engines buried in the fuselage.

The tests were conducted in the Langley 16-foot transonic tunnel at Mach numbers from 0.70 to 1.08 and at angles of attack from -2° to 7°. The test Reynolds number per foot varied from 3.57×10^6 to 4.35×10^6.

SYMBOLS

$\bar{c}$ mean aerodynamic chord, in.

$C_{A,i}$ internal axial-force coefficient, $\frac{\text{Internal axial force}}{qS}$

C_D drag coefficient, $\frac{\text{Drag}}{qS}$

C_D' drag coefficient based on unit area

C_L lift coefficient, $\frac{\text{Lift}}{qS}$

C_{L_α} lift-curve slope per deg, $\frac{dC_L}{d\alpha}$

C_m pitching-moment coefficient, $\frac{\text{Pitching moment}}{qS\bar{c}}$

$C_{m_{C_L}}$ longitudinal stability parameter, $\frac{dC_m}{dC_L}$

$C_{p,b}$ fuselage or nacelle base-pressure coefficient, $\frac{p_b - p_\infty}{q}$

L/D lift-drag ratio

M free-stream Mach number

m/m_∞ inlet mass-flow ratio based on inlet capture area

p static pressure, lb/sq ft

q free-stream dynamic pressure, lb/sq ft

S reference area, sq ft

α angle of attack referred to wing chord plane, deg

Λ wing sweep referred to wing leading edge or 50-percent chord, deg

Subscripts:

b fuselage or nacelle base

∞ free stream

max maximum

min minimum

APPARATUS AND PROCEDURE

Wind Tunnel and Support System

The Langley 16-foot transonic tunnel is a single-return atmospheric wind tunnel with a slotted test section of octagonal cross-sectional shape. The speed of this tunnel ranges from a Mach number of 0.20 to 1.10 and can be varied continuously by changing the tunnel drive power.

The models were sting mounted and supported by a strut extending through the test-section floor. The entire system was pivoted in such

a manner that the models remained on or near the tunnel center line throughout the angle-of-attack range.

Models

Sketches and photographs showing the general arrangements of the three 5-percent-scale models are given in figures 1 to 7. Other pertinent geometrical parameters, not shown on the model sketches, are listed in table I. All models had internal flow ducts with the inlets sized for properly matched operation at a Mach number of 1.2.

Model 1 (figs. 1 to 3) was investigated with three slightly different fuselage shapes. The basic, full-length configuration was tested with a sting cover plate installed on the bottom of the afterbody (model 1, fig. 3(a)). This plate was used to contour properly the original afterbody, which had been slotted to accommodate a different sting than the one actually used. Tests were also made without the cover plate in order to determine its aerodynamic effects (model 1A, fig. 3(b)). In addition, the model was investigated with a shortened nose section but only with the cover plate installed (model 1B, fig. 1).

The second variable-sweep configuration (figs. 4 and 5) used the same wing as model 1 and a very similar tail arrangement, the major differences being the afterbody shape and nacelle installation. Tests were conducted with the nacelles in two different vertical positions, the lower being derived from the basic position of model 2 by incorporating negative dihedral and additional length in the nacelle mounting struts (model 2A, fig. 4(b)). The longitudinal and lateral positions of the nacelles remained unchanged.

The "skewed-wing" configuration, designated model 3 (figs. 6 and 7), had a fuselage similar to that of model 1, with engines located in the afterbody. In this case, however, the planform was to be varied by rotating a straight, tapered wing about a central pivot. The unusual tail arrangement was necessary to provide adequate longitudinal stability with the wing skewed 90° (fully retracted). Like the previous variable-sweep configurations, model 3 was tested with the wing fully retracted.

In addition to the complete-model configurations described, models 1 and 3 were also tested with the horizontal- and vertical-tail surfaces removed. A summary of all configurations is given in table II.

Normal cross-sectional-area distributions of the major configurations are shown in figures 8 to 10. On each of these plots, approximately 83 percent of the total inlet capture area has been deleted over the length of the internal ducting. This increment represents the effective internal flow area based on an average measured mass-flow ratio for each model.

Instrumentation

A six-component internal strain-gage balance was used to determine the forces and moments on the models. The electrical outputs from the balance were transmitted to self-balancing potentiometers, converted to digital form, and punched into cards. Total and static pressures from rake surveys of the duct or nacelle exits, and static pressures in the base and balance cavity of each model were measured with mercury manometers. The pressure data were photographically recorded during the investigation and later punched into cards.

Tests

Force and moment data were obtained for each model configuration at Mach numbers from 0.70 to 1.08. Since the minimum drag characteristics were of primary importance, data were only taken over a relatively small angle-of-attack range. For model 1, the angles varied from about -2° to 7°; for model 2, from about -2° to 4°, and for model 3, from about -2° to 6°. Maximum and minimum values of test Reynolds number per foot are plotted against Mach number in figure 11. The only wing settings investigated were the 80° sweep position of models 1 and 2 and the 90° skewed position of model 3. No attempt was made to trim the models for any particular flight condition.

Boundary-layer transition was fixed on each model by strips of No. 180 carborundum grain 0.125 inch wide located 1 inch behind the nose and 0.25 inch behind the leading edge of the wing and tail surfaces. For models 1 and 3, similar strips were also positioned about 1 inch in back of the inlet lips, and for model 2, approximately 0.5 inch behind the nacelle inlets and leading edges of the nacelle support struts.

In another series of runs completely separate from those of the force tests, rake surveys were made of the static and total pressures in the duct exits, and the static pressures over the base and balance cavity areas of the models were also determined. The resulting mass-flow ratios, internal axial-force coefficients, and base-pressure coefficients, appear in figures 12, 13, and 14, respectively.

Corrections and Accuracies

All drag data have been adjusted to the condition of free-stream static pressure existing at the base of the fuselage or nacelles and in the balance cavity. For model 1A the base correction also includes the area of a small step which existed at the forward end of the afterbody slot when the sting cover plate was removed. Corrections to the drag have also been made for axial forces caused by the internal flow. (See

fig. 13.) The angle of attack, measured from the wing chord plane, has been corrected for both flow angularity and sting support deflections caused by aerodynamic loads.

On the basis of the known characteristics of the instrumentation and data reduction procedures, the data are estimated to be accurate to within the following limits:

M_∞	±0.005
α, deg	±0.15
C_L	±0.01
C_D	±0.0005
C_m	±0.005

Some force data were obtained at angles of attack beyond the range covered by the base and internal corrections, and extrapolations of the pressure data were sometimes necessary. Since these data vary only moderately with angle of attack, any resulting errors should be small. The drag accuracy quoted is, however, only applicable to the angle range shown in figures 12 to 14.

PRESENTATION OF RESULTS

The results of this investigation are presented in the following figures:

	Figure
Longitudinal aerodynamic characteristics:	
Model 1	15
Model 1, tails off	16
Model 1A	17
Model 1B	18
Model 2	19
Model 2A	20
Model 3	21
Model 3, tails off	22
Variation of C_{L_α} with Mach number:	
Models 1, 1 (tails off), 1A, and 1B	23
Models 2 and 2A	24
Models 3 and 3 (tails off)	25

DISCUSSION

Lift and Pitching-Moment Characteristics

The basic models were all longitudinally stable over the transonic speed range and exhibited low lift-curve slopes. (Low lift-curve slopes are essential in minimizing gust loads during low-altitude supersonic flight.) The average value of lift-curve slope between Mach numbers of 0.90 and 1.08 generally varied from 0.03 to 0.045 for the different models, based on individual wing area. (See figs. 23 to 25.) Over the same speed range the longitudinal stability parameter $C_{m_{C_L}}$ varied from -0.2 to -0.3 for model 1, from -0.1 to -0.16 for model 2, and from -0.5 to -0.7 for model 3. (See figs. 26 to 28.) Within the limited angle-of-attack range of the investigation, maximum values of untrimmed lift-drag ratio could only be obtained for model 1, and these values varied from a maximum subsonic level of 7.6 to approximately 5.6 at low supersonic speeds. (See fig. 29.)

Modifications made to the fuselage of model 1 involving the sting cover plate or the short nose section had no significant effect on lift-curve slopes or the longitudinal stability parameter. (See figs. 23 and 26.) Lowering the nacelles on model 2 produced no change in lift-curve slope but did reduce the stability of this configuration at transonic speeds. (See figs. 24 and 27.)

Comparing the data for models 1 and 3 with and without tail surfaces shows that the wing-body component of the variable-sweep configuration

provided most of the total lift and significant stabilizing effect at positive lift coefficients. (See figs. 15 and 16.) However, the wing-body combination of the skewed-wing configuration, having almost no exposed wing area behind the moment center, produced little more than half the total lift and was unstable. (See figs. 21, 22, 25, and 28.)

Minimum Drag Characteristics

The minimum drag coefficients presented in figures 30 to 32 are based on the individual wing area of each configuration. These figures generally show that the critical Mach number for all models was approximately 0.90 and that the drag-rise increments at $M = 1.08$ ranged from 50 to 70 percent of the subsonic drag level.

A comparison of the minimum drag of models 1 and 1B (fig. 30) shows that shortening the nose section with the sting cover plate installed caused no appreciable change in subsonic drag or critical Mach number and only increased the drag rise slightly.

The difference in the drag characteristics of models 1 and 2 can be attributed primarily to the influence of the engine installation on the shape of the rear 50 to 60 percent of the fuselage, since the remaining components of the two configurations are very similar, if not identical. Less drag rise was achieved with the tapered-afterbody—nacelle combination than with the broad fuselage shape of model 1. (See figs. 30, 31, and 33.) Although neither of the nacelle positions investigated was necessarily an optimum with regard to aerodynamic interference, a slight reduction in drag rise was obtained by displacing the nacelles vertically to the position of model 2A. (See figs. 31 and 33.) Subsequent tests of a similar configuration involving different lateral and longitudinal nacelle positions tend to show that lateral position may have the largest influence on drag at transonic speeds (unpublished data). Although model 2 provided less drag rise, the overall drag for this particular configuration was higher than that of model 1 at all Mach numbers. (See figs. 30, 31, and 33.)

In order to show the relative merits of the various configurations for a given mission, namely, that of low-level supersonic dash, the Drag/q (that is, $C_{D,min}'$) of the various models has been computed and results presented in figure 33. As might be expected from the lower fineness ratio of model 3, the transonic drag rise was greater than that of models 1 and 2. This condition resulted in model 3 having a slightly higher drag than model 1 at a Mach number of 1.08.

In view of the general interest in the effects on drag of altering model afterbody contours for wind-tunnel support systems, it should also

be noted that the drag of model 1A (underportion of afterbody slotted) was conservative with respect to that of model 1. (See fig. 30.) This effect is attributed to the adverse influence of the slot on afterbody pressure recovery as indicated by the base-pressure data in figure 13(a). Furthermore, unpublished data from a more recent investigation tend to show that the drag of afterbodies with large fairings between the jet exits may be similarly affected when the lower portion of the fairing is removed to accommodate a sting.

SUMMARY OF RESULTS

A transonic investigation of three V/STOL fighter models with fully retracted variable-sweep or skewed wings and different engine installations showed the following results:

1. All complete models were longitudinally stable and exhibited low lift-curve slopes.

2. The critical Mach number for all configurations was approximately 0.90, and the drag-rise increments ranged from 50 to 70 percent of the subsonic drag level.

3. The model with nacelles suspended from the fuselage afterbody produced less transonic drag rise than a comparable configuration with the jet exits located in the base; however, the overall drag was higher for the podded-engine configuration at all Mach numbers.

Langley Research Center,
National Aeronautics and Space Administration,
Langley Station, Hampton, Va., June 5, 1962.

REFERENCES

1. Bielat, Ralph P., Robins, A. Warner, and Alford, William J., Jr.: The Transonic Aerodynamic Characteristics of Two Variable-Sweep Airplane Configurations Capable of Low-Level Supersonic Attack. NASA TM X-304, 1960.

2. Bielat, Ralph P., and Robins, A. Warner: Stability and Control Characteristics at Transonic Speeds of Two Variable-Sweep Airplane Configurations Differing in Wing-Pivot Locations. NASA TM X-559, 1961.

3. Spearman, M. Leroy, and Robinson, Ross B.: Stability and Control Characteristics at a Mach Number of 2.01 of a Variable-Sweep Airplane Configuration Capable of Low-Level Supersonic Attack - Outer Wing Swept 75°. NASA TM X-310, 1960.

4. Robinson, Ross B., and Howard, Paul W.: Stability and Control Characteristics at a Mach Number of 1.41 of a Variable-Sweep Airplane Configuration Capable of Low-Level Supersonic Attack - Outer Wing Swept 75° and 108°. NASA TM X-320, 1960.

5. Robinson, Ross B., and Spearman, M. Leroy: Stability and Control Characteristics at a Mach Number of 2.2 of a Variable-Sweep Airplane Configuration Capable of Low-Level Supersonic Attack - Outer Wing Swept 75°. NASA TM X-330, 1960.

6. Bielat, Ralph P., and Pierpont, P. Kenneth: Transonic Aerodynamic Characteristics of a Variable-Sweep Airplane Configuration Having a 12-Percent-Thick Wing and an Inboard Pivot Location. NASA TM X-429, 1960.

7. Robinson, Ross B., and Howard, Paul W.: Stability and Control Characteristics at a Mach Number of 2.2 of a Variable-Sweep Airplane Configuration Having a 12-Percent-Thick Wing Swept 75° and an Inboard Pivot Location. NASA TM X-435, 1960.

8. Ward, Robert J.: Transonic Aerodynamic Characteristics at a Wing Sweep of 104° of a Variable-Sweep Airplane Configuration With an Over-and-Under Engine Installation. NASA TM X-444, 1961.

9. Luoma, Arvo A.: Longitudinal Aerodynamic Characteristics at Transonic Speeds of Two V/STOL Airplane Configurations With Skewed and Variable-Sweep Wings. NASA TM X-527, 1961.

10. Morris, Odell A., and Foster, Gerald V.: Static Longitudinal and Lateral Aerodynamic Characteristics at a Mach Number of 2.20 of a V/STOL Airplane Configuration With a Variable-Sweep Wing and With a Skewed Wing Design. NASA TM X-521, 1961.

TABLE I.- MODEL GEOMETRICAL PARAMETERS

	Model 1	Model 2	Model 3
Wing:			
Area, sq ft	1.2075	1.2075	1.000
Mean aerodynamic chord, in.	12.80	12.80	7.20
Aspect ratio	1.25	1.25	0.59
Incidence angle, deg	1.0	1.0	0
Dihedral angle, deg	0	0	0
Airfoil sections	64A207 Normal to T.E.	64A207 Normal to T.E.	5 percent (upper) Flat (lower)
Horizontal tail:			
Area (exposed), sq ft	0.227	0.213	0.226
Incidence angle, deg	0	0	0
Airfoil sections	65A003	65A003	64A004.35 (root) 64A002 (tip)
Vertical tail:			
Area (exposed), sq ft	0.252	0.205	0.212
Dihedral angle (from vertical), deg	0	0	30
Airfoil sections	65A003	65A003	64A004 (root) 64A002 (tip)
Miscellaneous:			
Approximate external wetted area, sq ft	5.80	6.17	4.863
Total inlet capture area, sq ft	0.0185	0.0246	0.0194
Total duct exit area, sq ft	0.0190	0.0246	0.0194

TABLE II.- SUMMARY OF MODEL CONFIGURATIONS

Model	Description	Configuration tested
1	Long nose; outboard pivot type wing with outer panels swept 80°; side inlets; engines located in fuselage afterbody; sting cover plate installed.	Complete model
		Horizontal and vertical tails removed
1A	Model 1 with sting cover plate removed.	Complete model
1B	Model 1 with short nose section and sting cover plate installed.	Complete model
2	Wing identical to that of model 1; engine nacelles on fuselage afterbody in upper position (nacelle-strut dihedral angle, 0°)	Complete model
2A	Model 2 with nacelles in lower position (nacelle-strut dihedral angle, -15.97°)	Complete model
3	"Skewed wing" with single, centrally located pivot; wing positioned with 50-percent-chord line parallel to stream; twin vertical stabilizers; side inlets; engines located in fuselage afterbody.	Complete model
		Horizontal and vertical tails removed

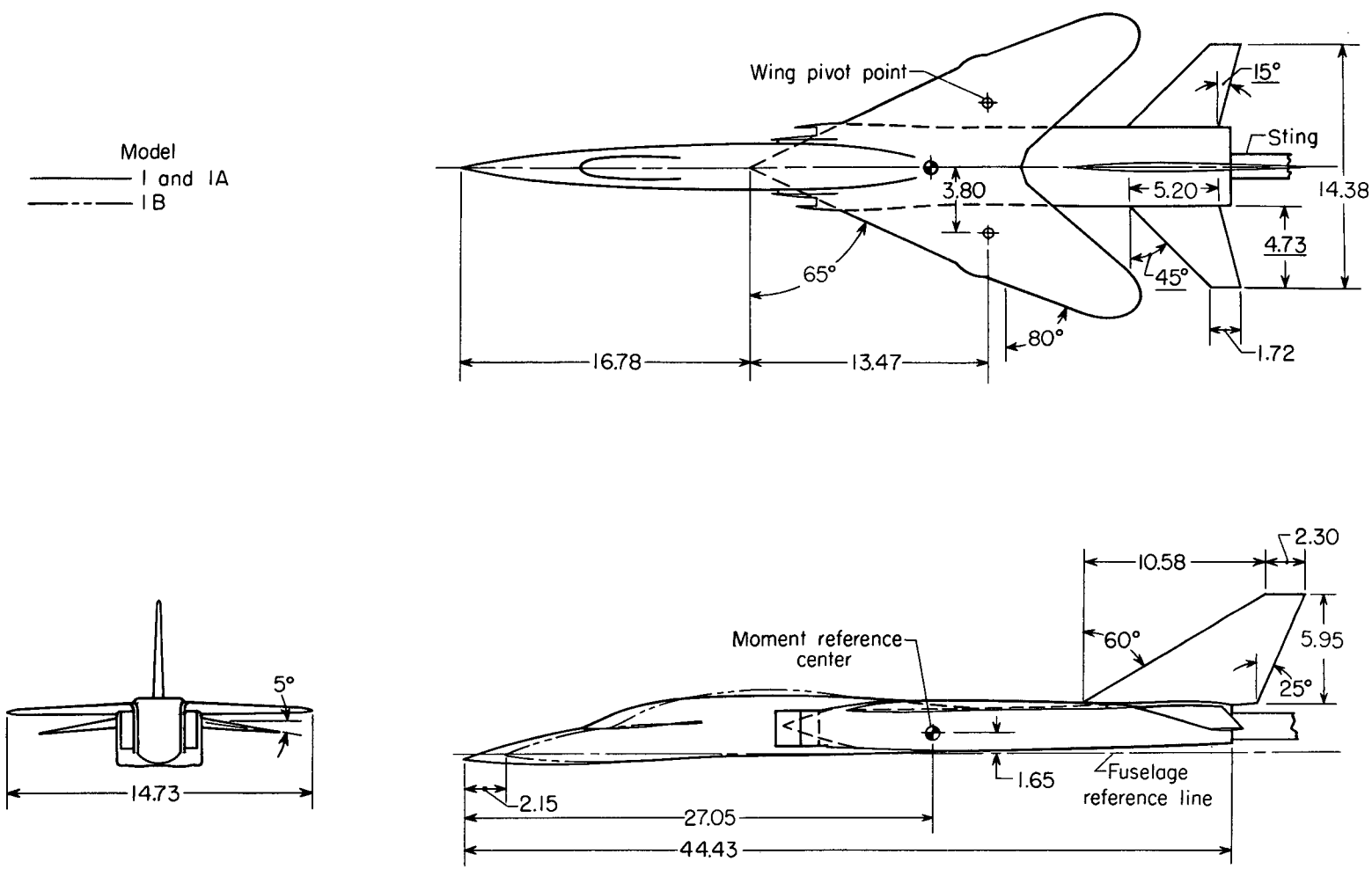

Figure 1.- Sketch of model 1. All dimensions are in inches unless otherwise noted. Underlined dimensions are in the plane of the horizontal tail.

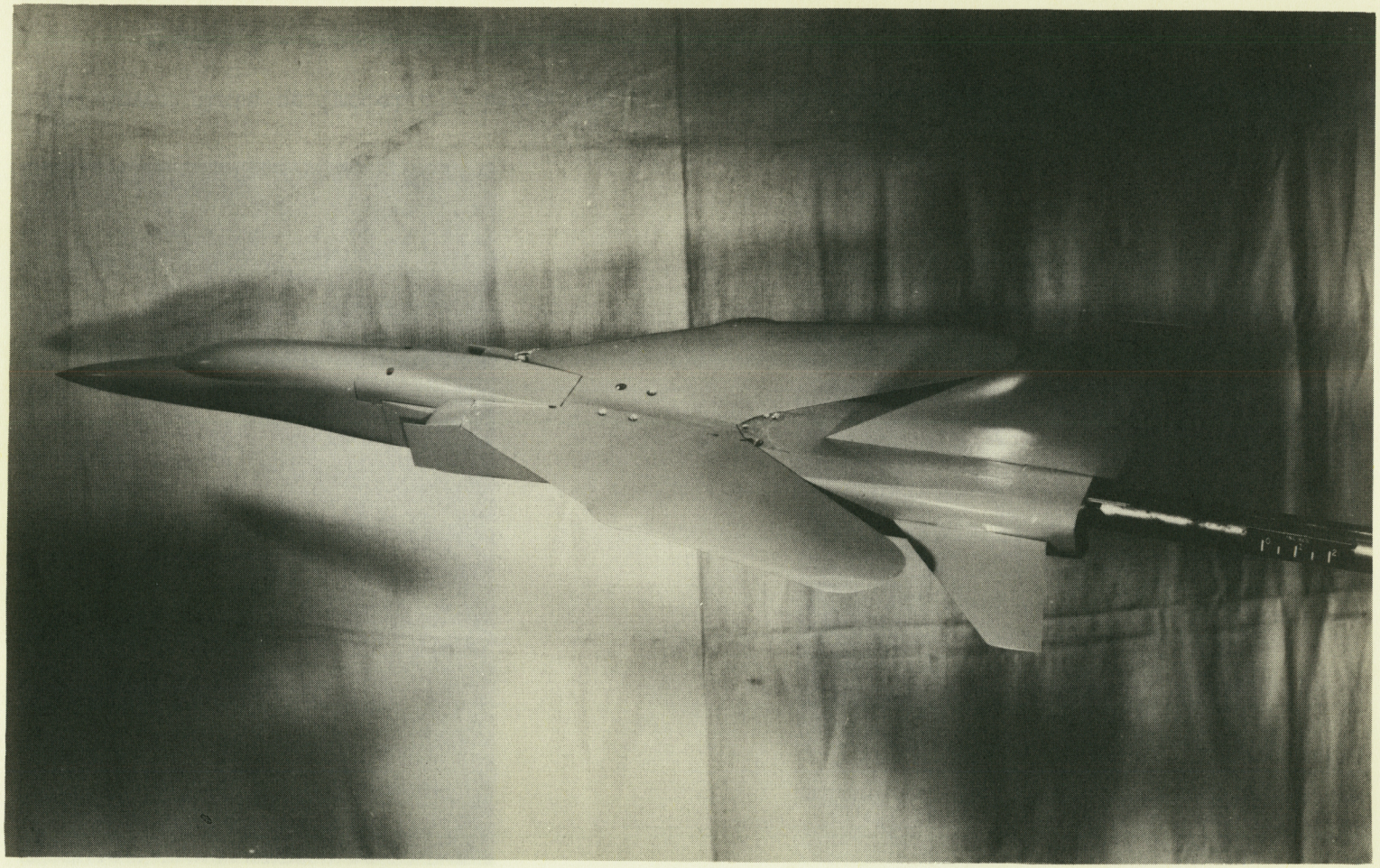

Figure 2.- Photograph of model 1. L-60-6863

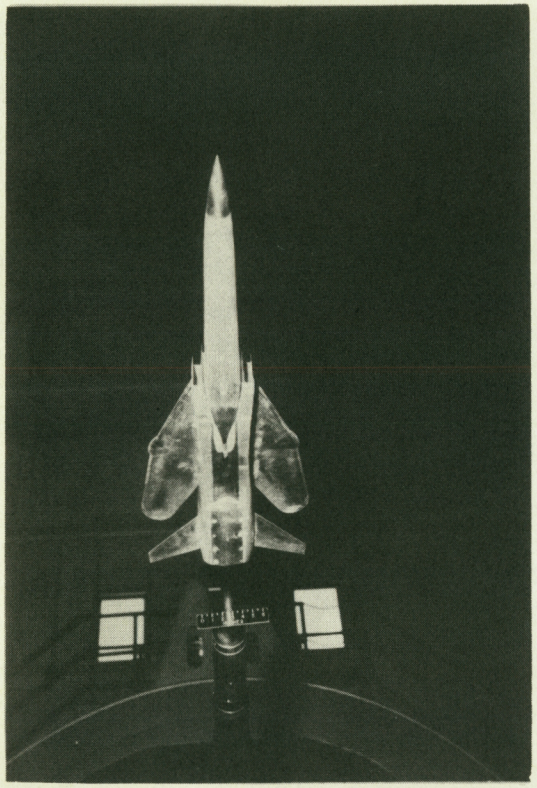

(a) Cover plate on (model 1). L-60-7932

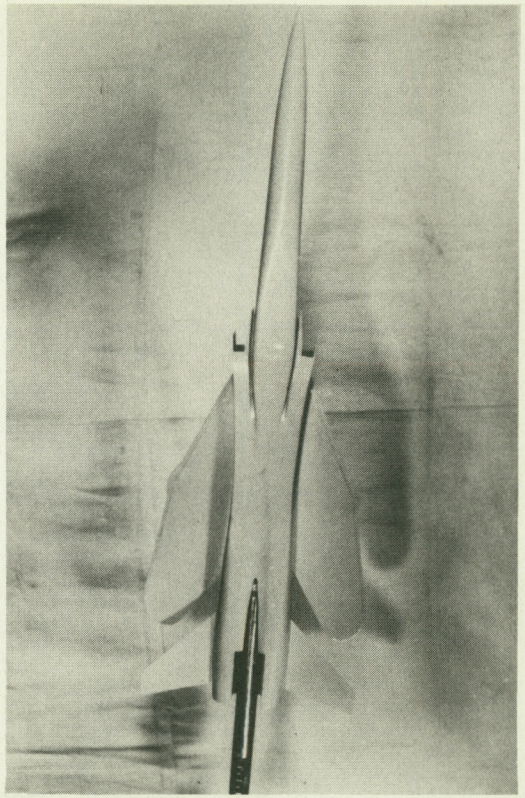

(b) Cover plate off (model 1A). L-60-6861

Figure 3.- Photographs showing differences between models 1 and 1A.

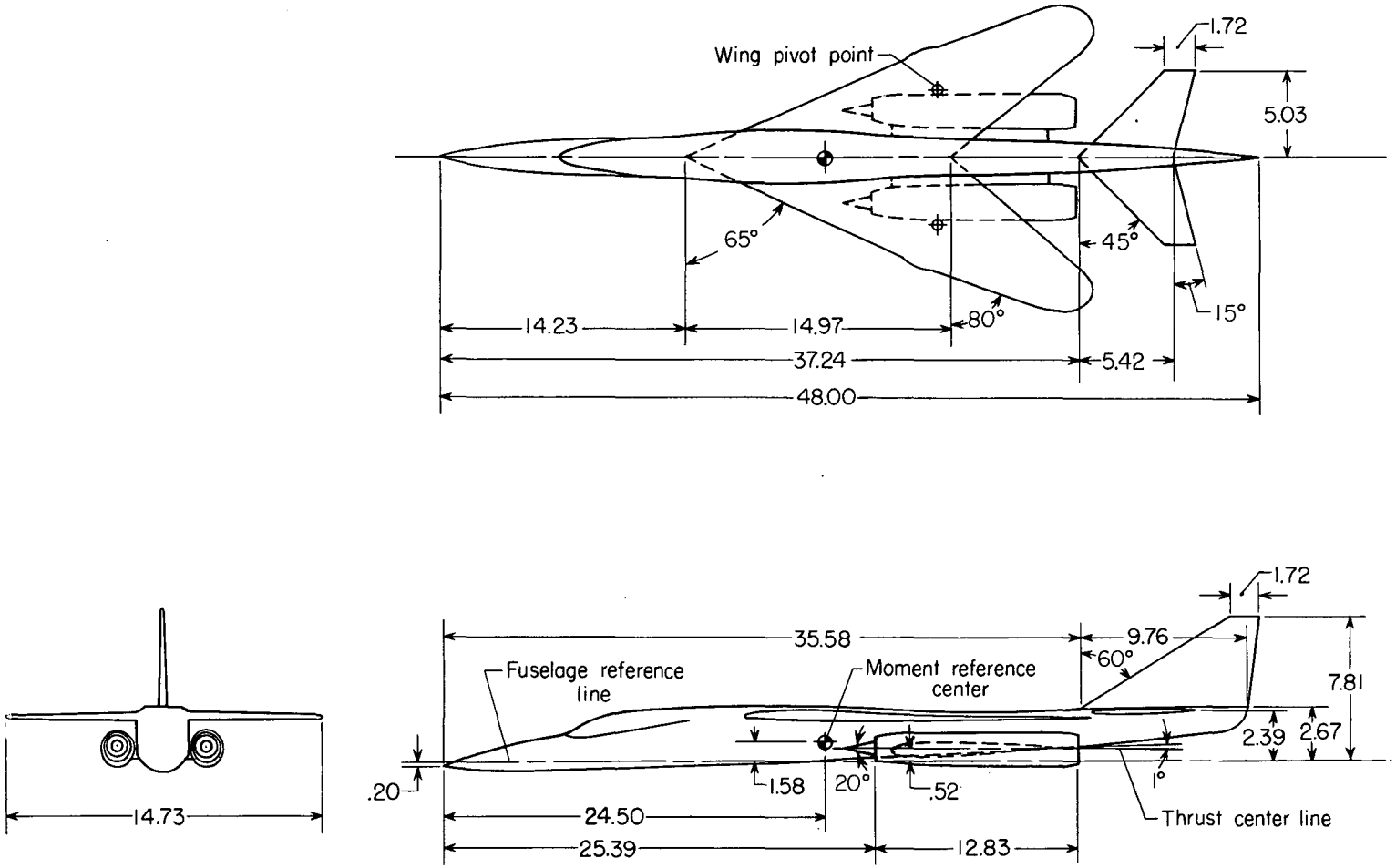

(a) Sketch of model 2.

Figure 4.- Sketch of model 2 and engine arrangement for models 2 and 2A. All dimensions are in inches unless otherwise noted.

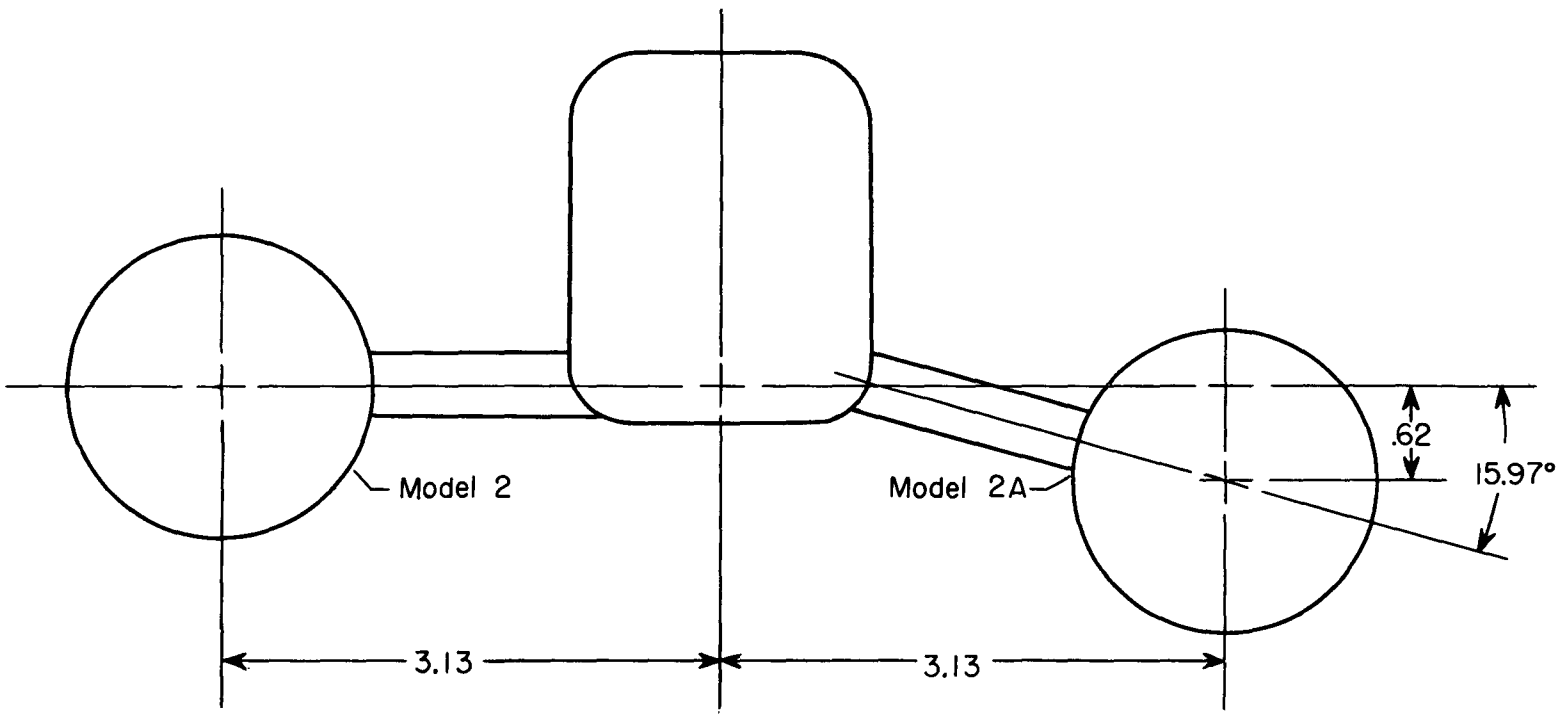

(b) Engine arrangement for models 2 and 2A.

Figure 4.- Concluded.

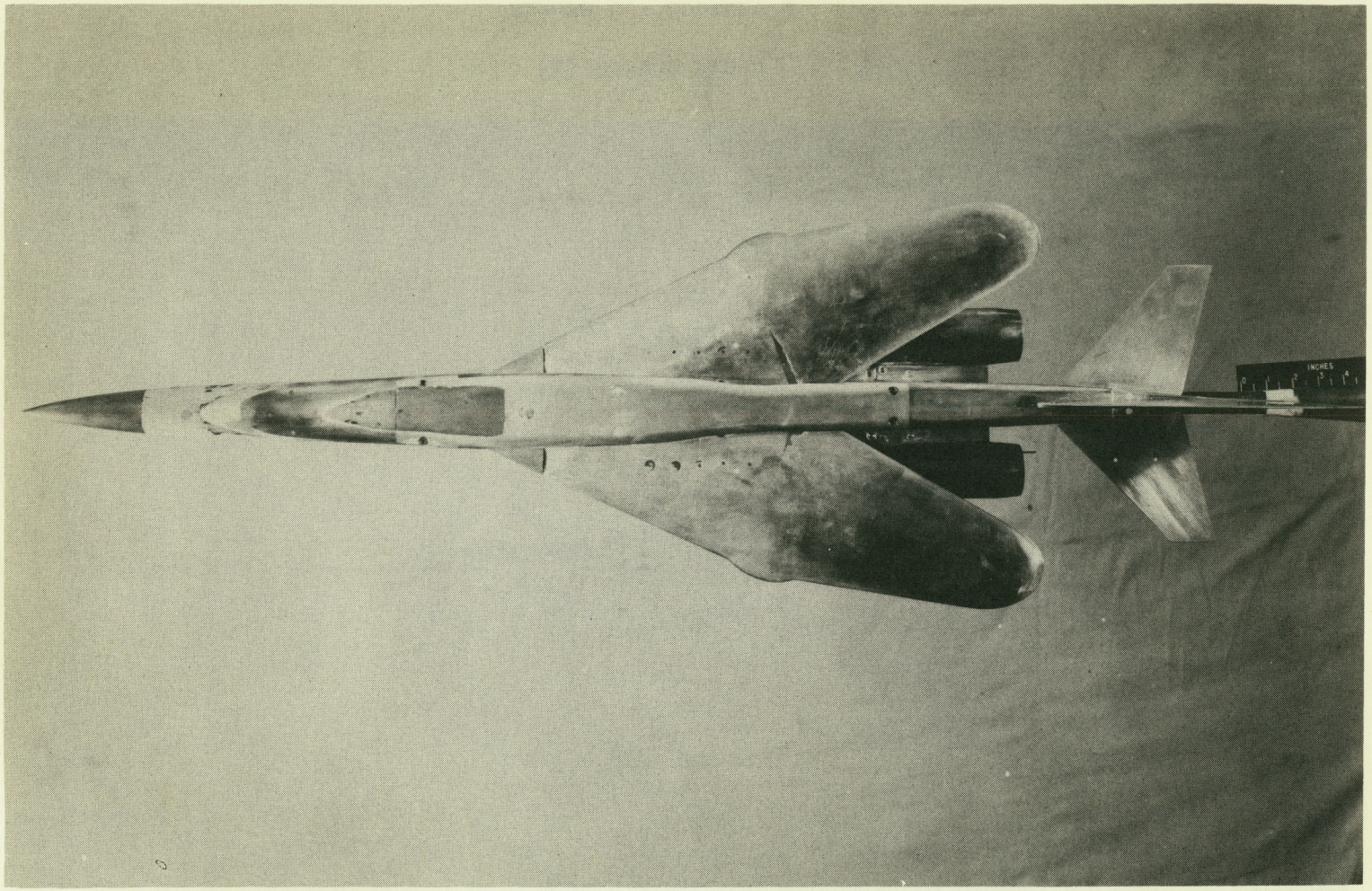

(a) Top view. L-61-6506

Figure 5.- Photograph of model 2.

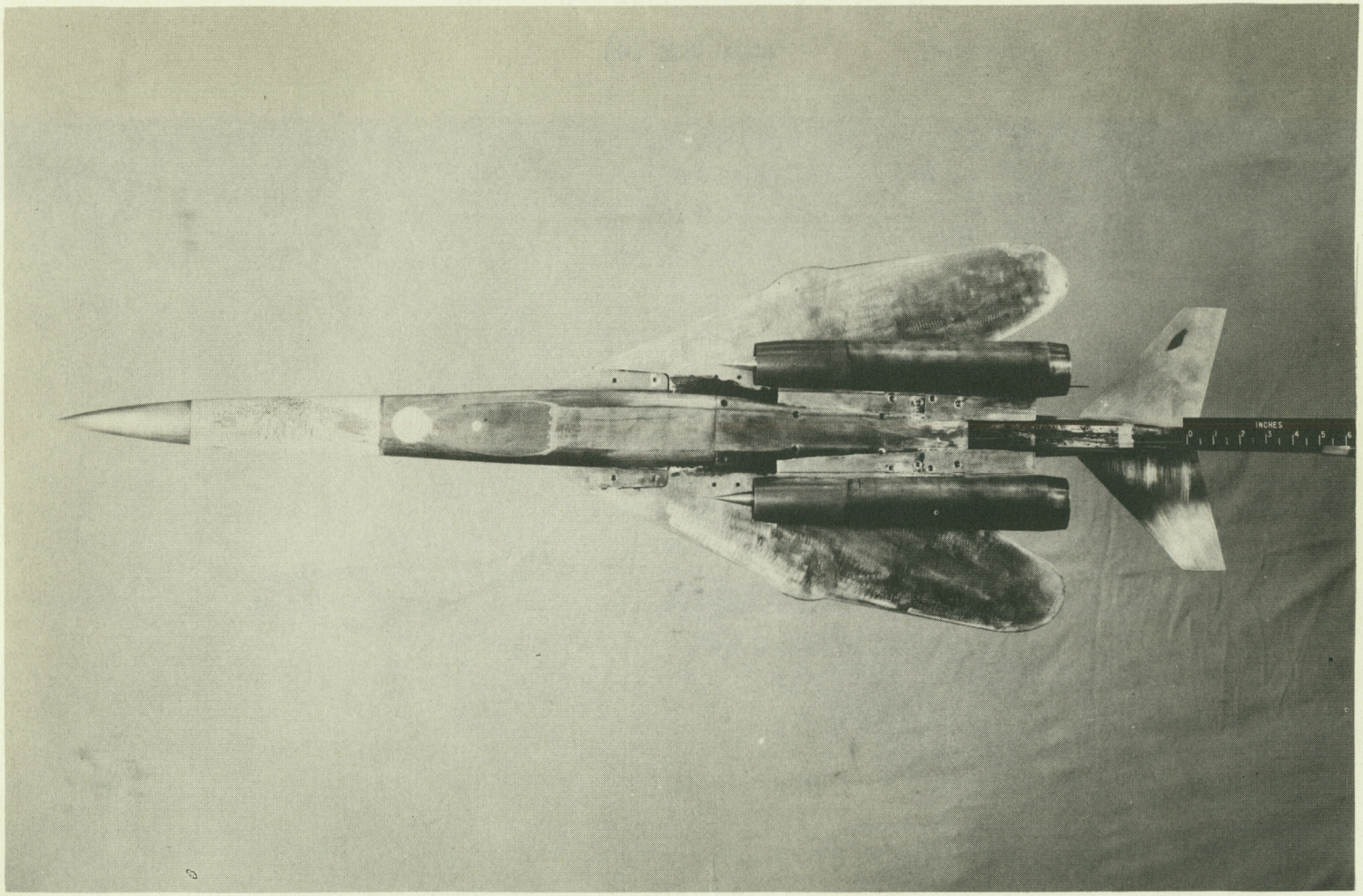

(b) Bottom view. L-61-6505

Figure 5.- Continued.

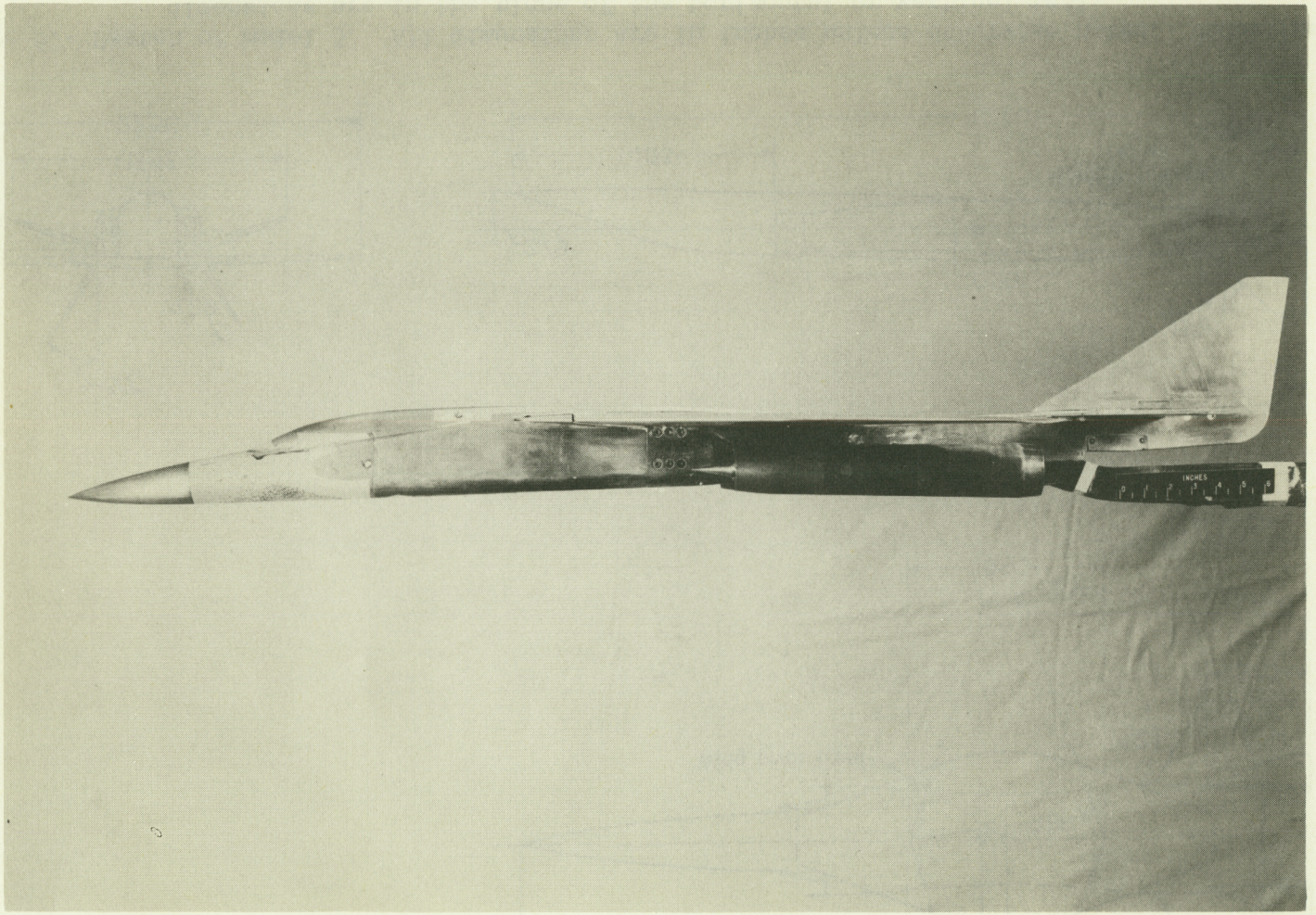

(c) Side view. L-61-6504

Figure 5.- Concluded.

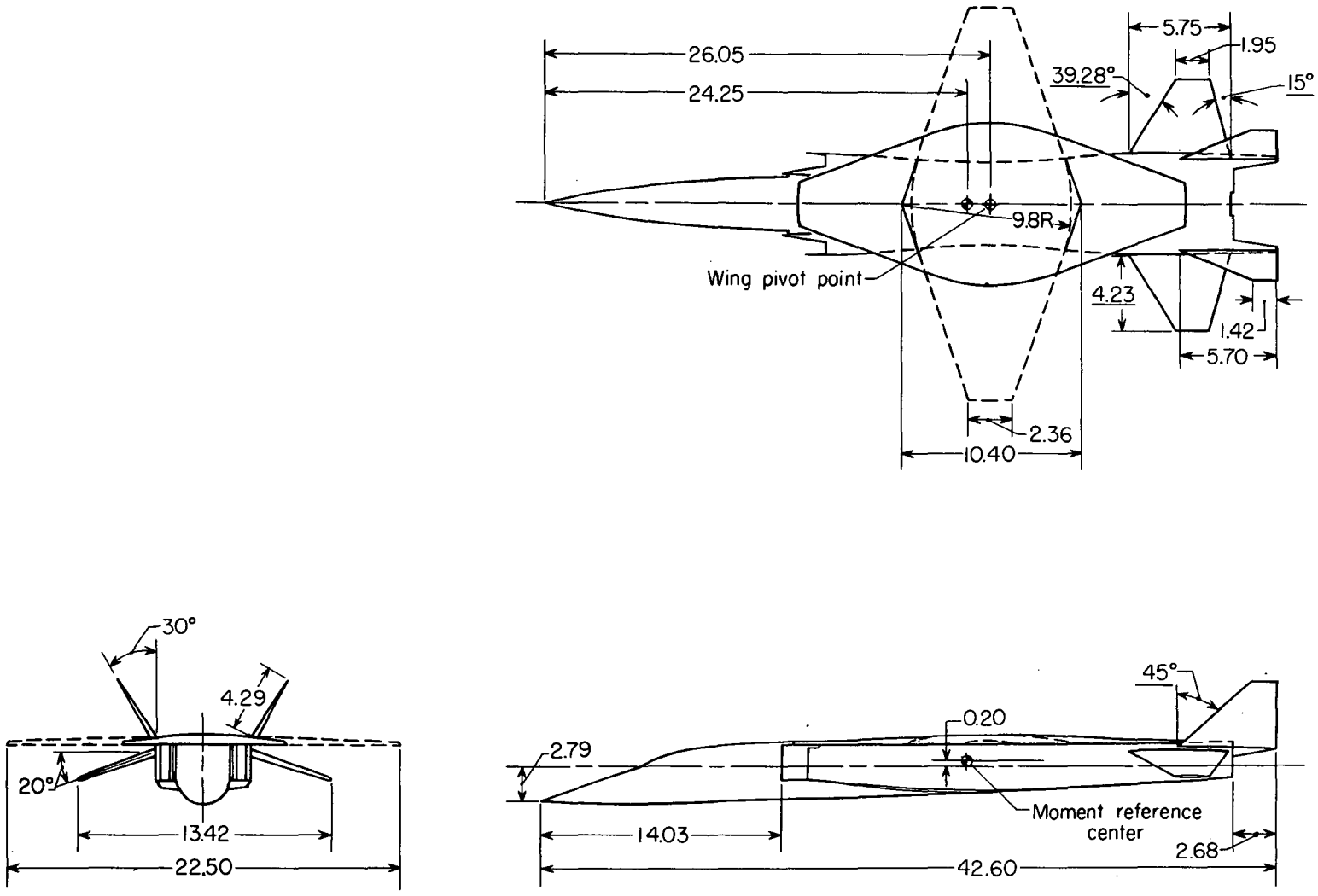

Figure 6.- Sketch of model 3. All dimensions are in inches unless otherwise noted. Underlined dimensions are in the plane of the horizontal or vertical tail.

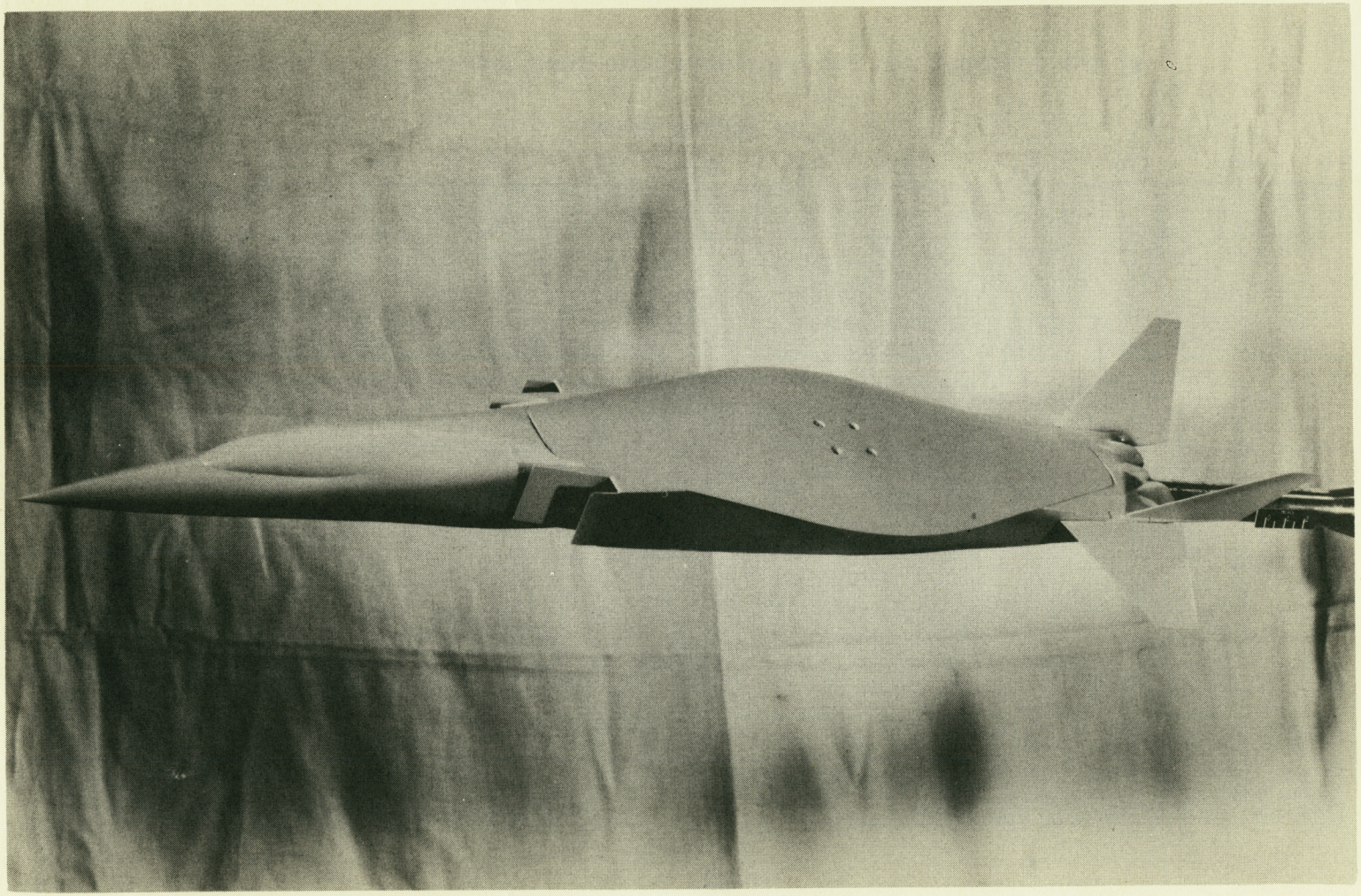

Figure 7.- Photograph of model 3. L-60-6859

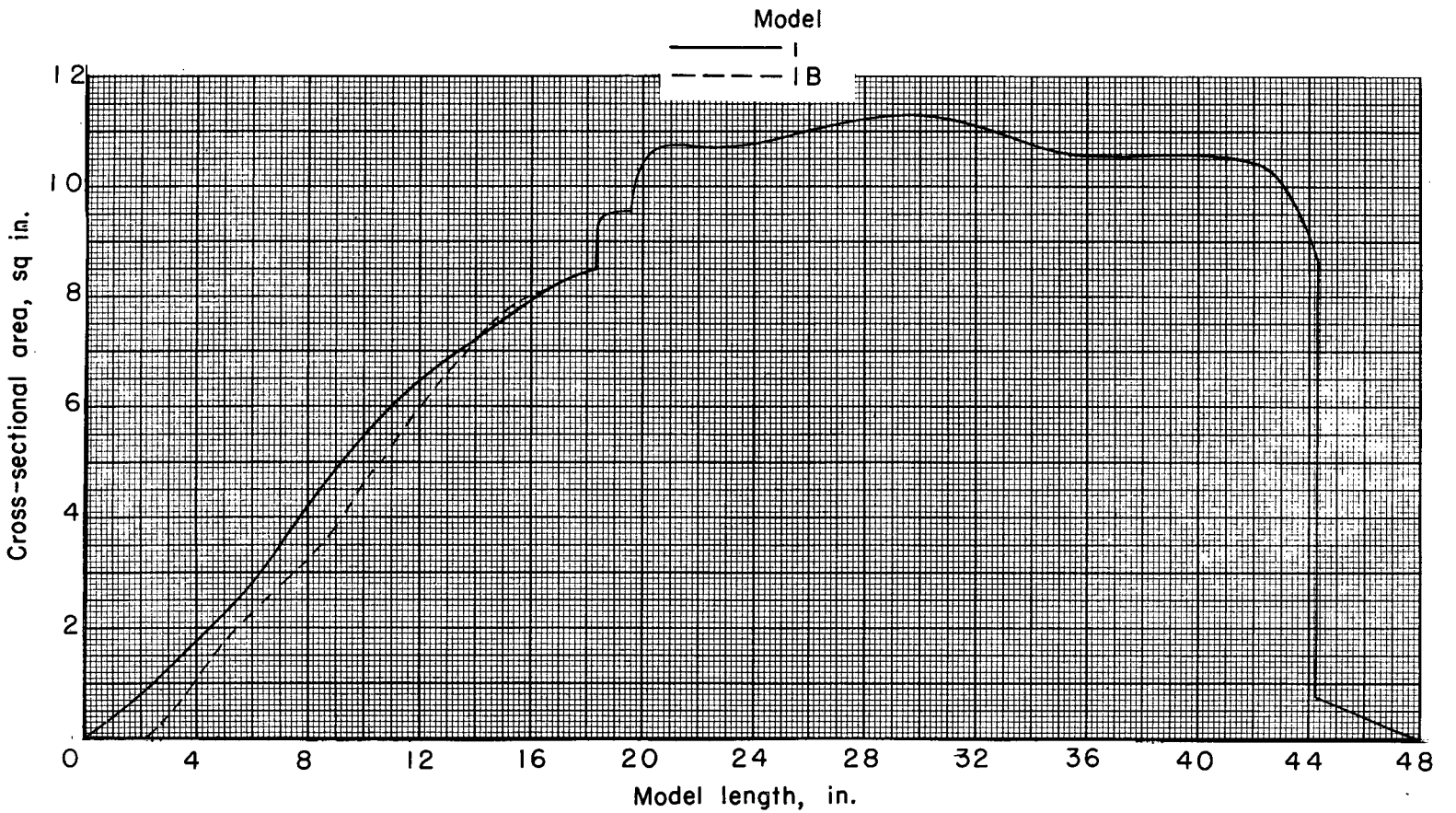

Figure 8.- Cross-sectional-area distributions for models 1 and 1B.

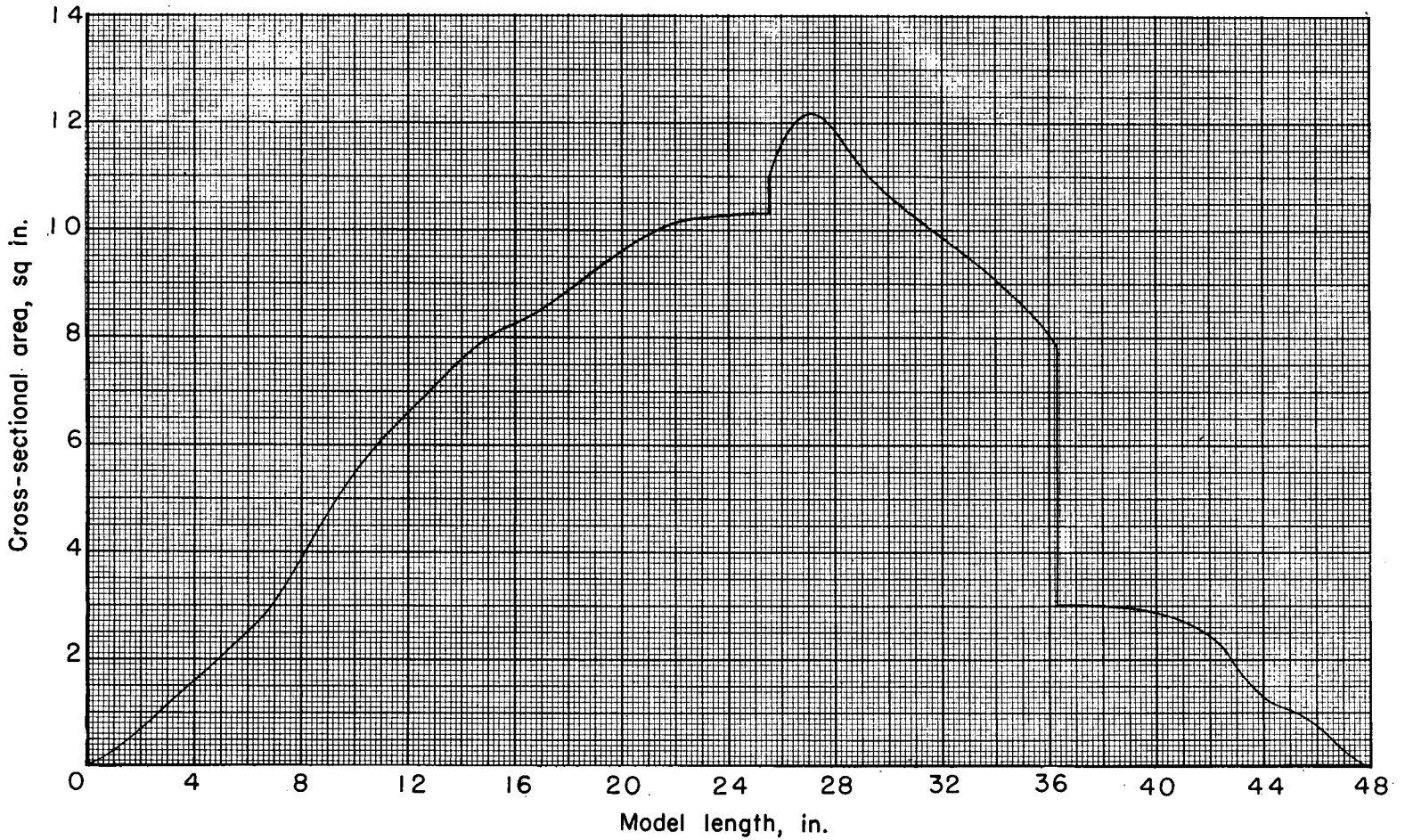

Figure 9.- Cross-sectional-area distributions for model 2.

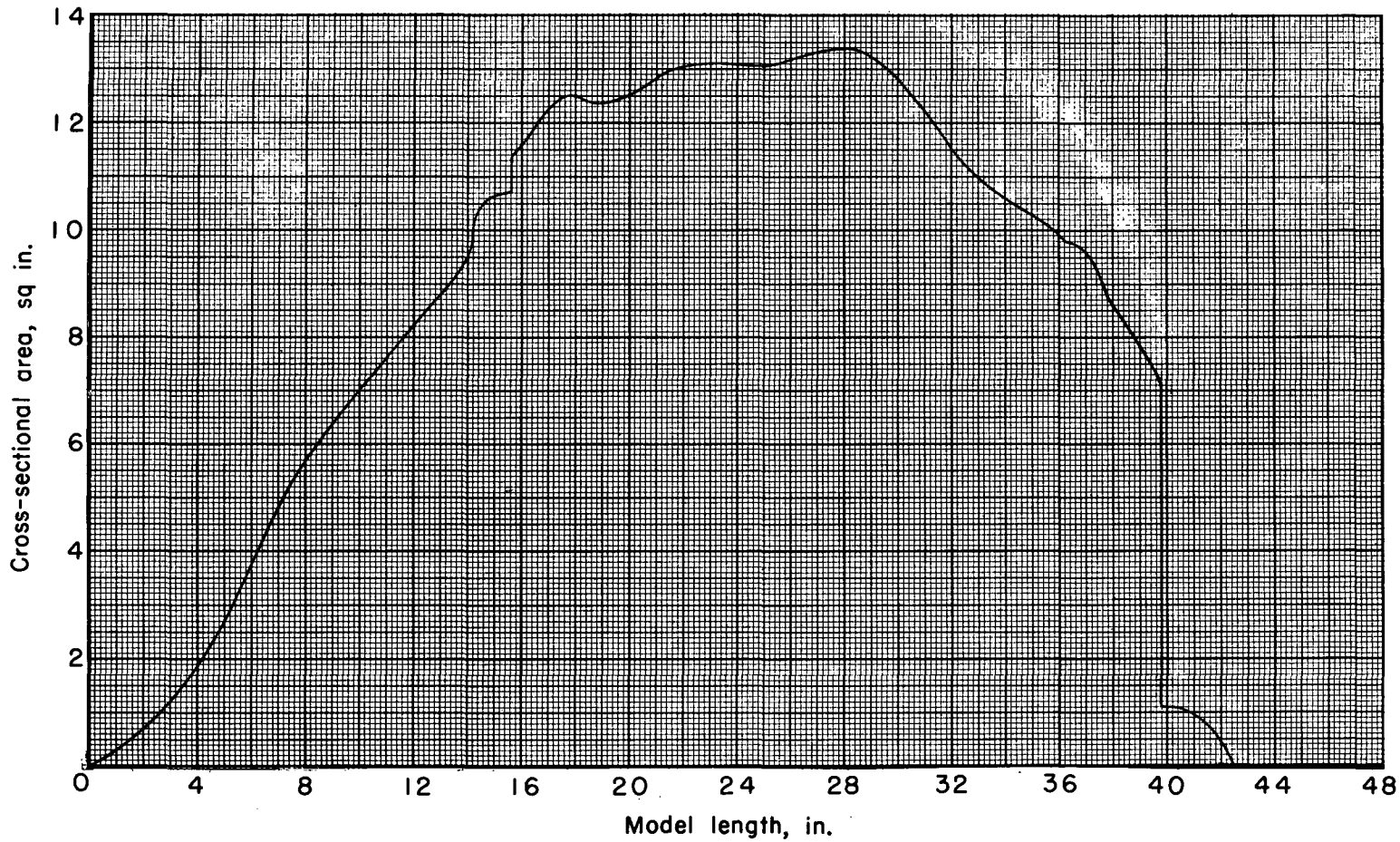

Figure 10.- Cross-sectional-area distributions for model 3.

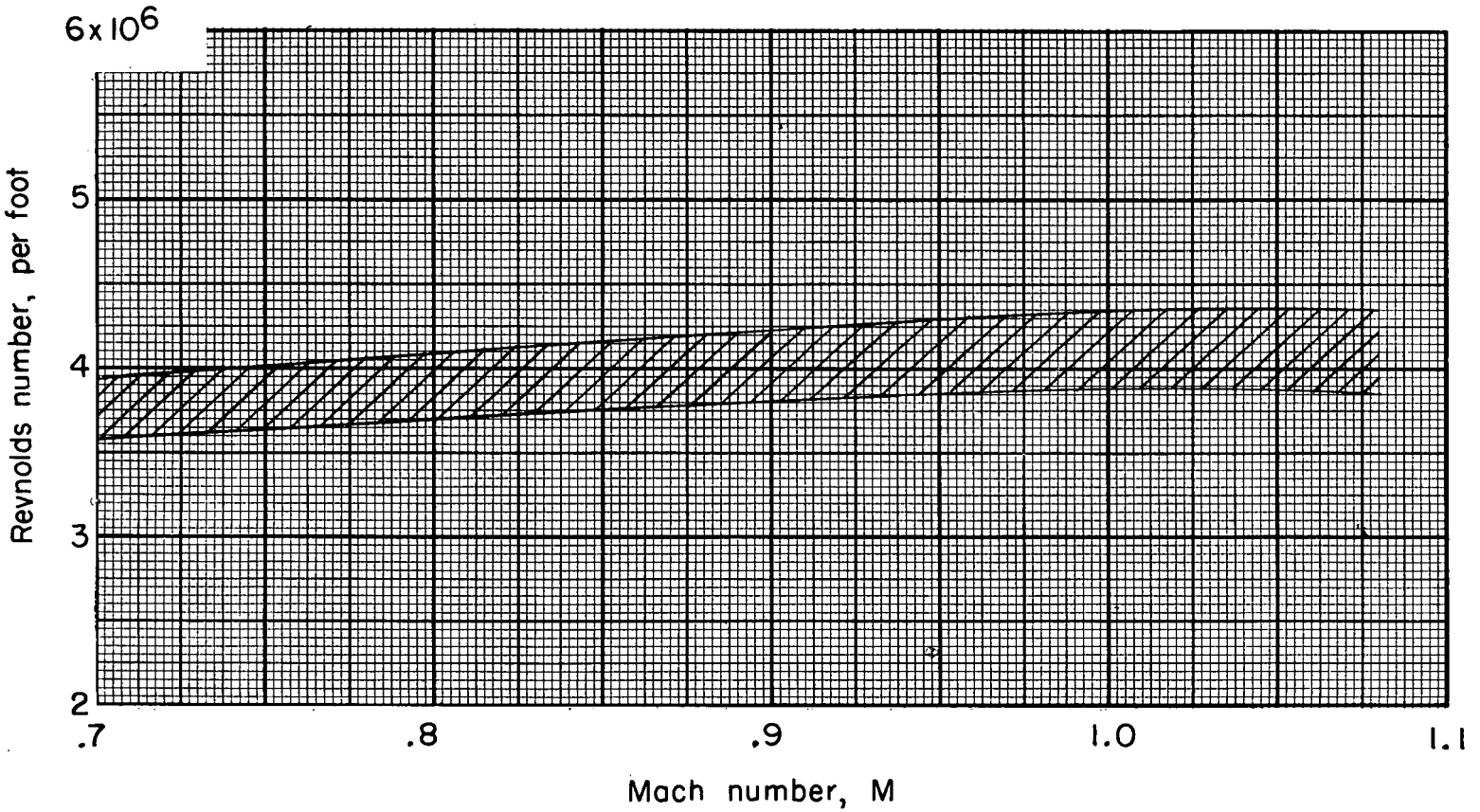

Figure 11.- Variation of test Reynolds number with Mach number.

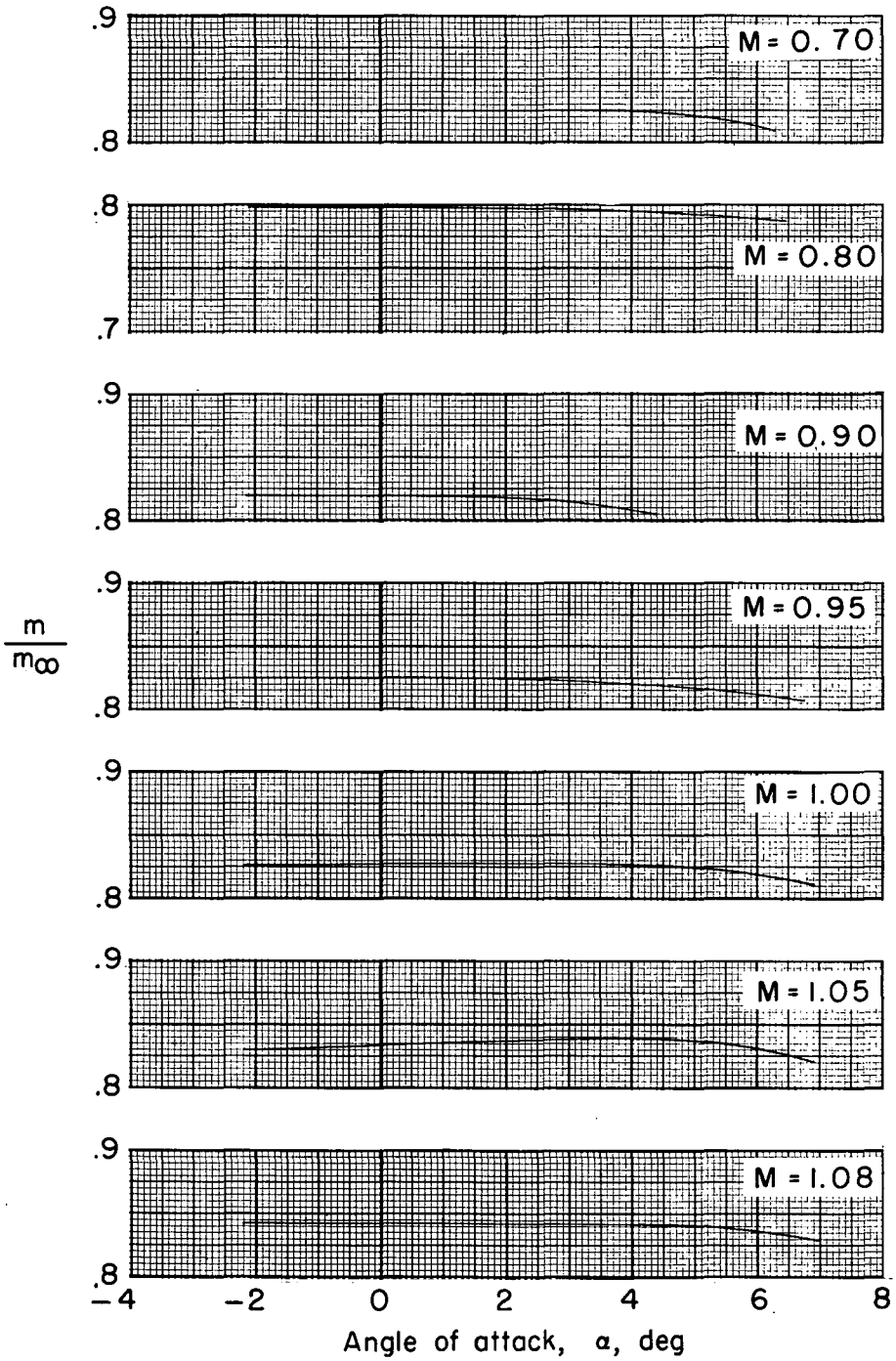

(a) Models 1, 1A, and 1B.

Figure 12.- Variation of mass-flow ratio with angle of attack.

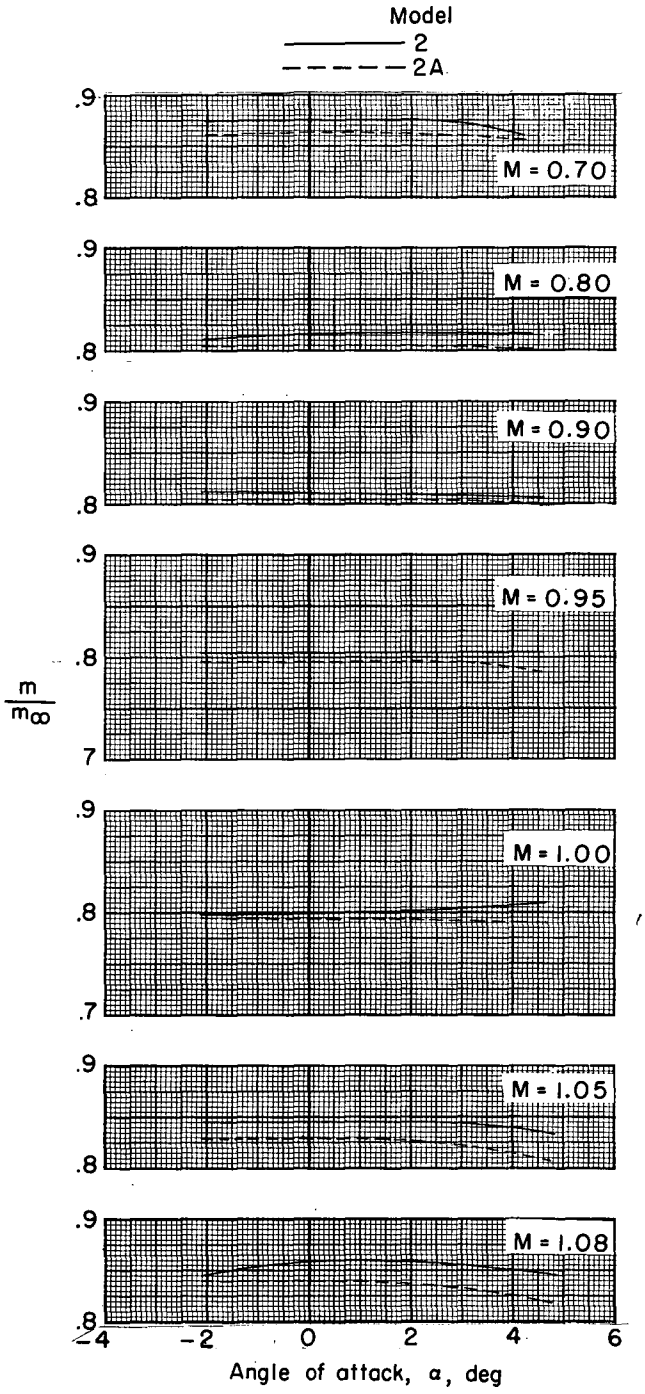

(b) Models 2 and 2A.

Figure 12.- Continued.

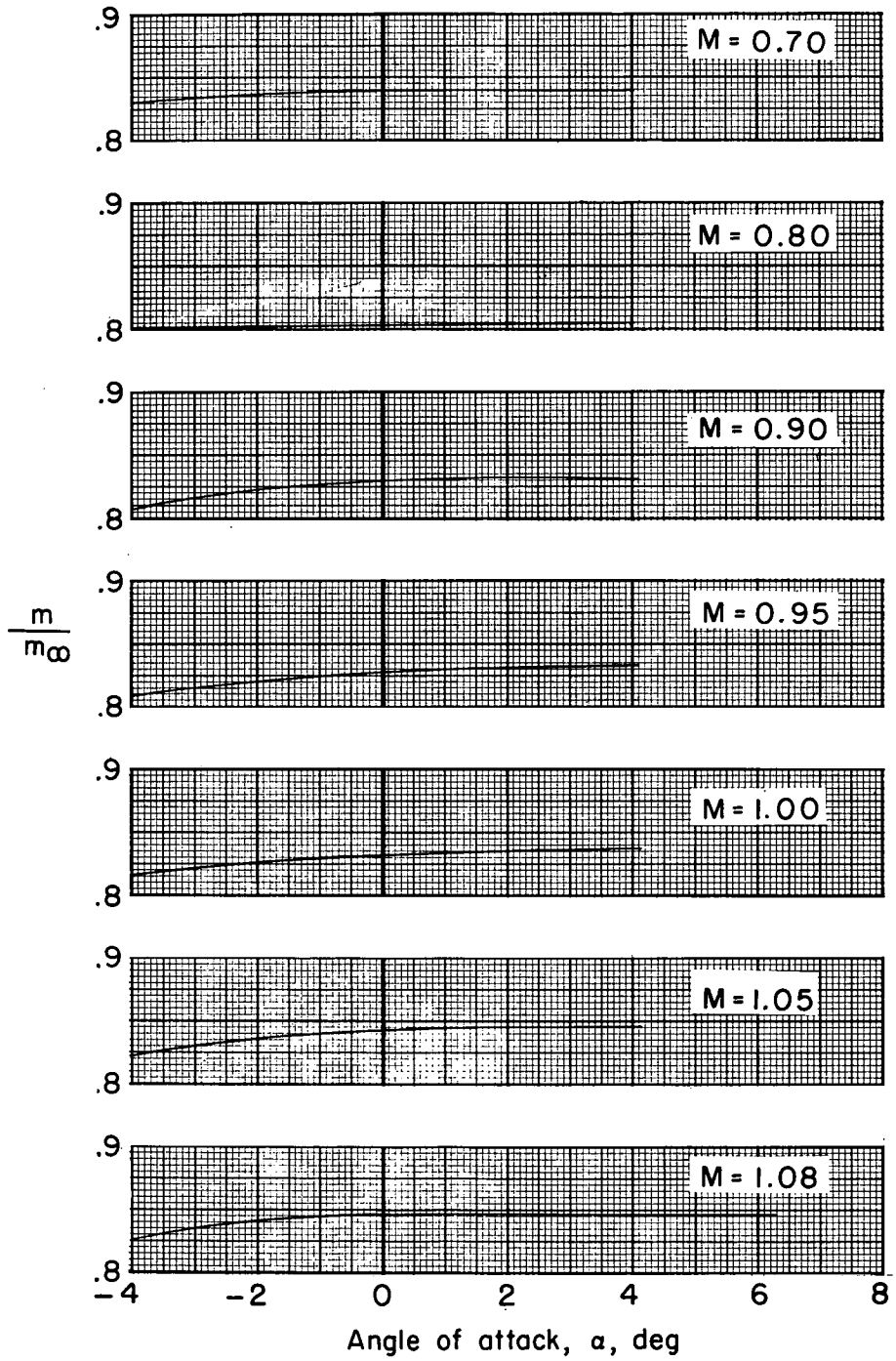

(c) Model 3.

Figure 12.- Concluded.

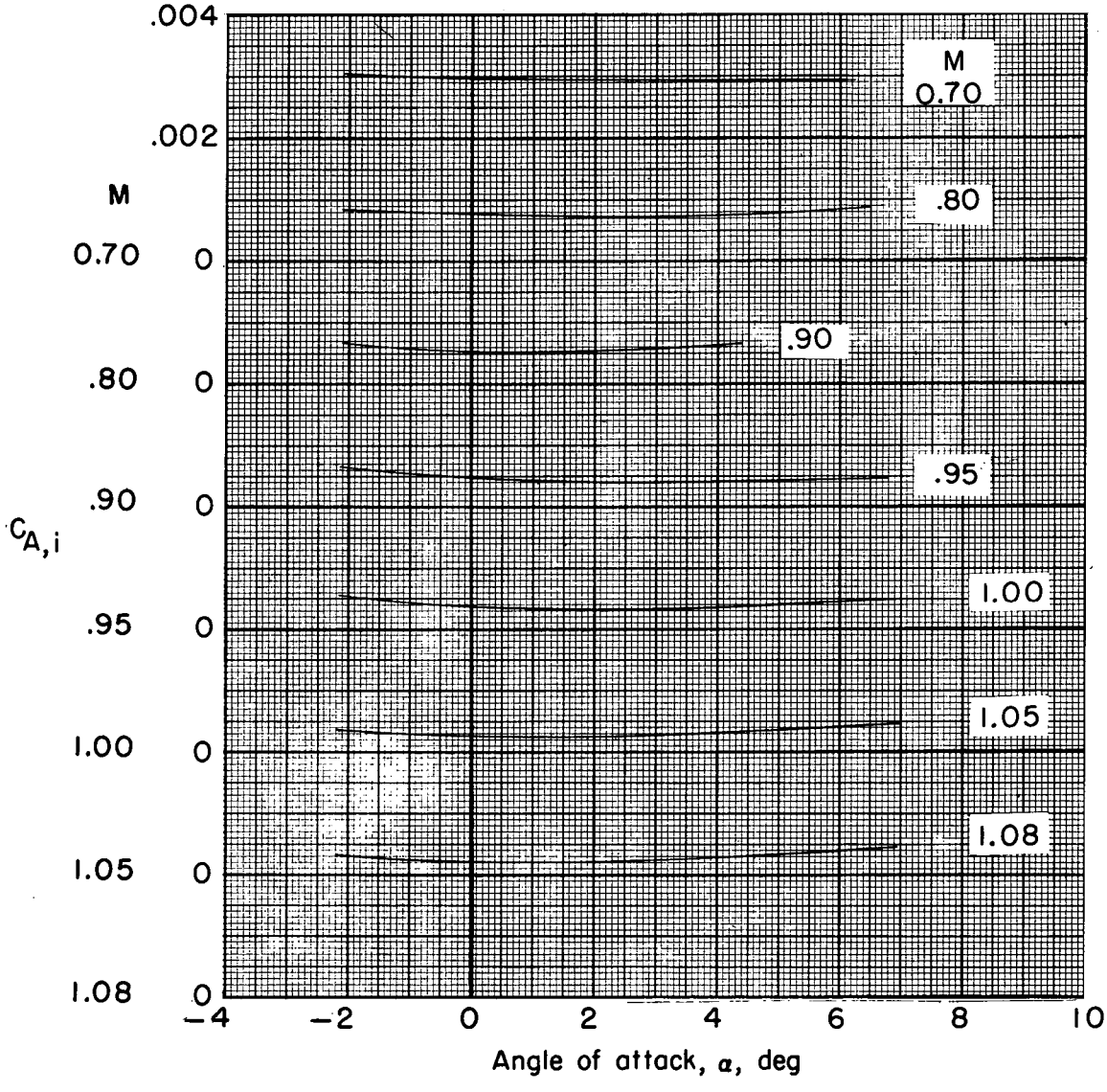

(a) Models 1, 1A, and 1B.

Figure 13.- Variation of internal axial-force coefficient with angle of attack.

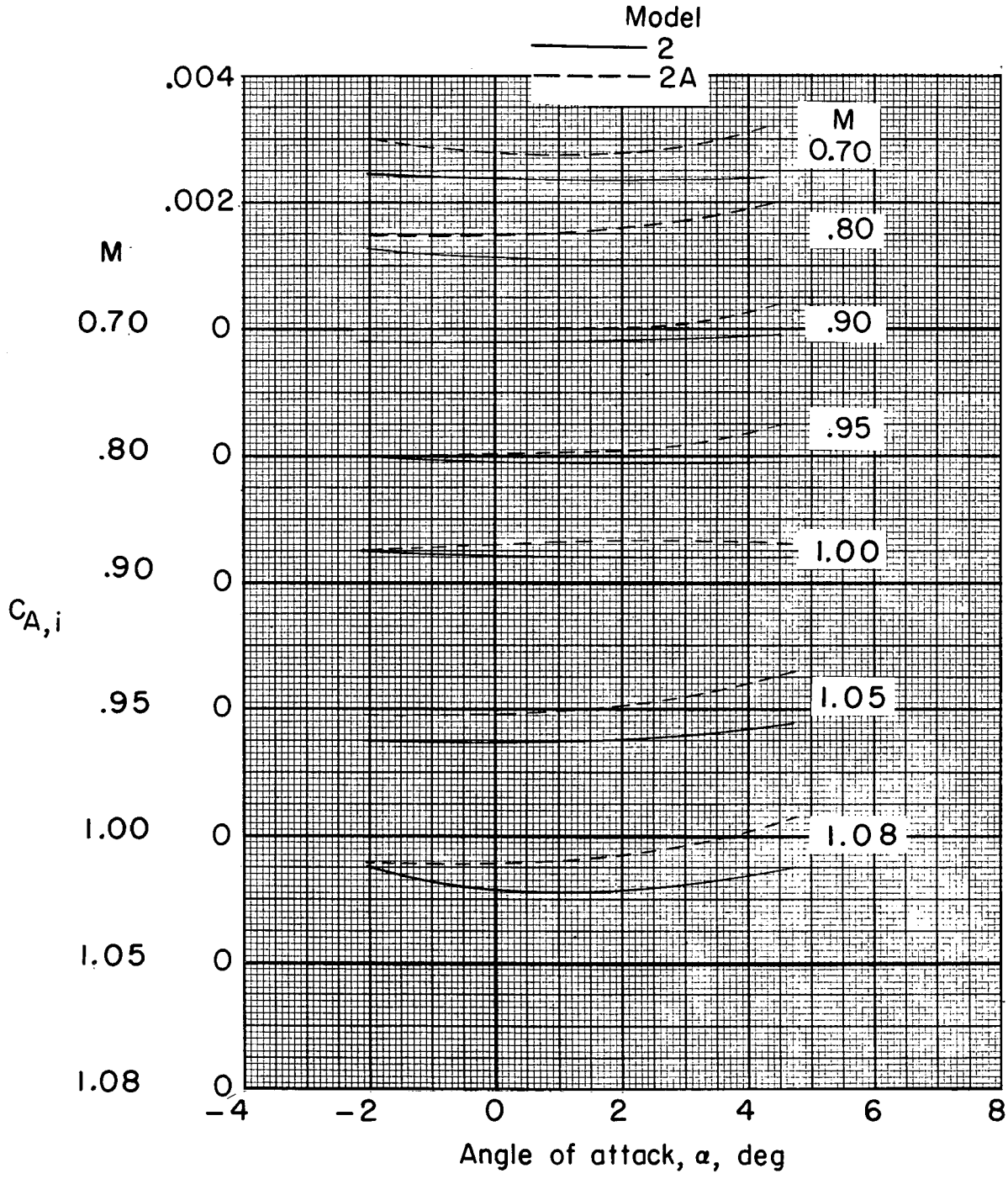

(b) Models 2 and 2A.

Figure 13.- Continued.

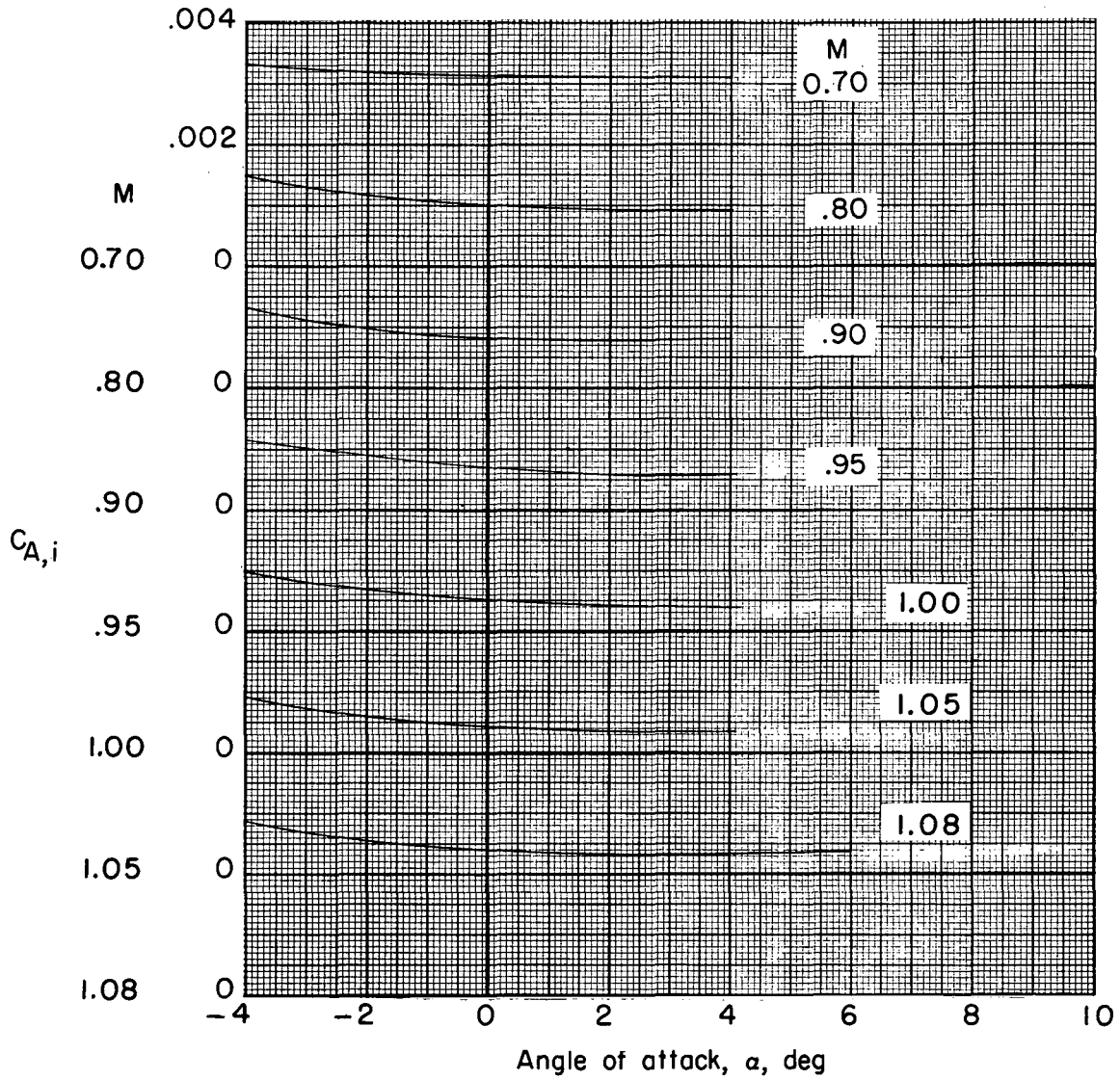

(c) Model 3.

Figure 13.- Concluded.

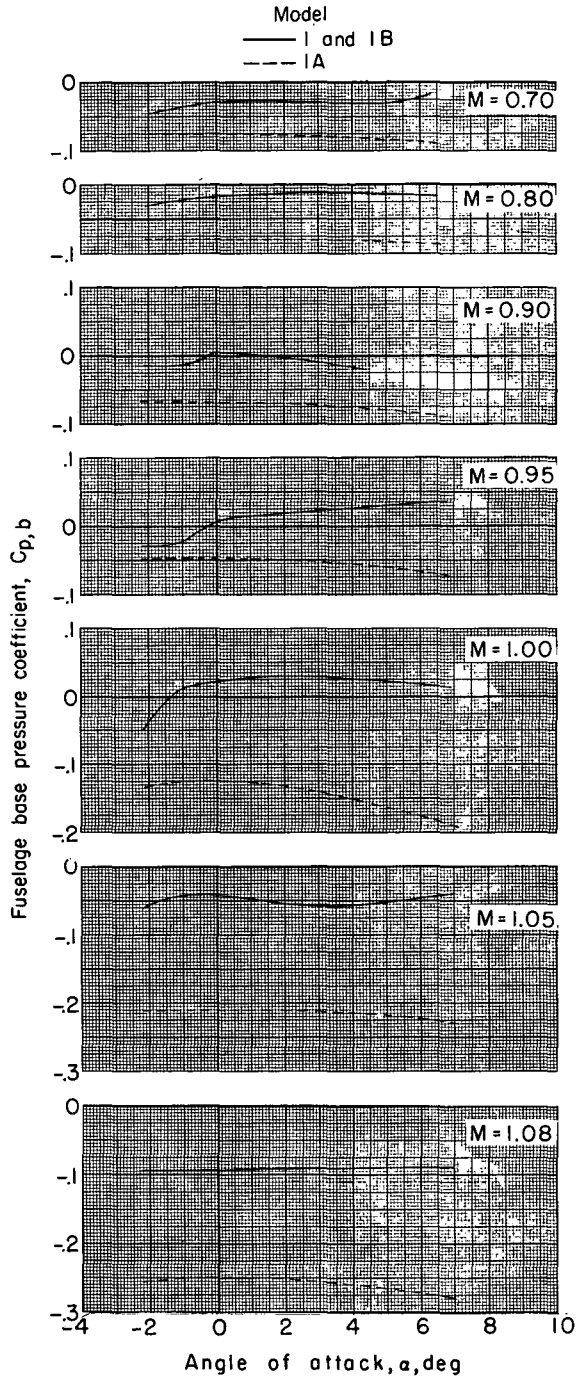

(a) Models 1, 1A, and 1B.

Figure 14.- Variation of fuselage or nacelle base-pressure coefficient with angle of attack.

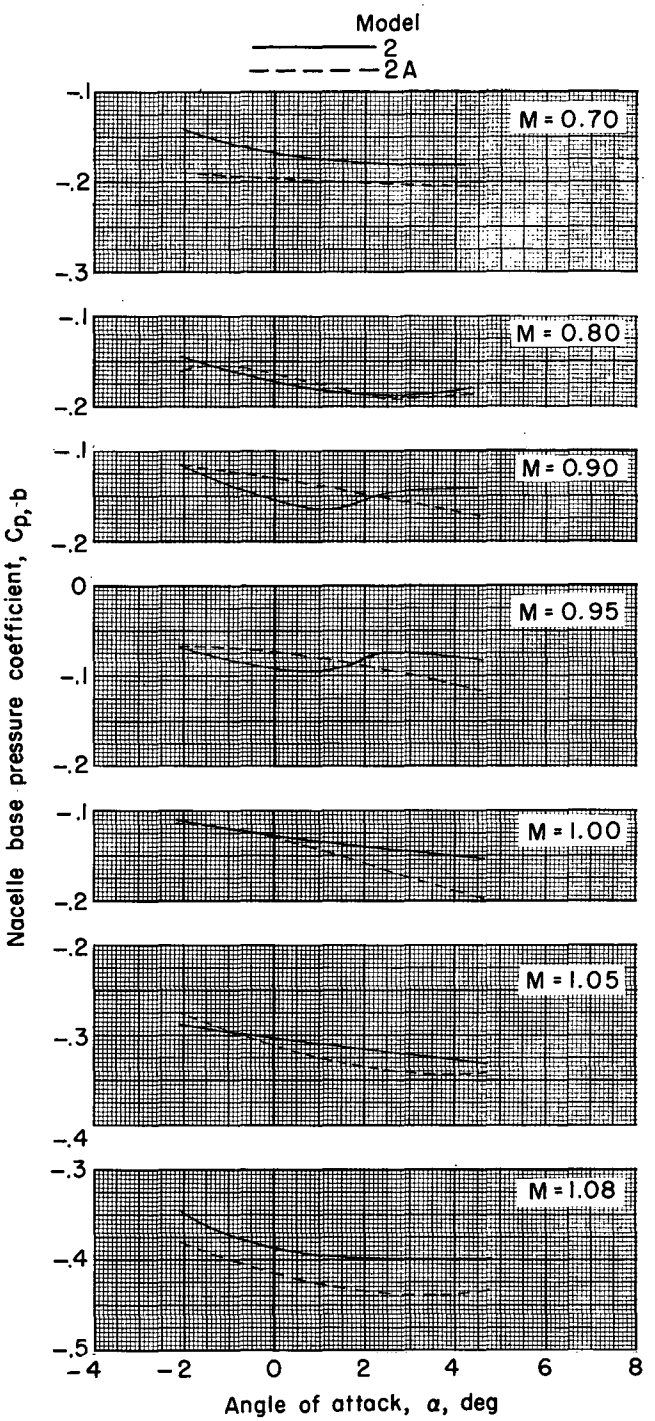

(b) Models 2 and 2A.

Figure 14.- Continued.

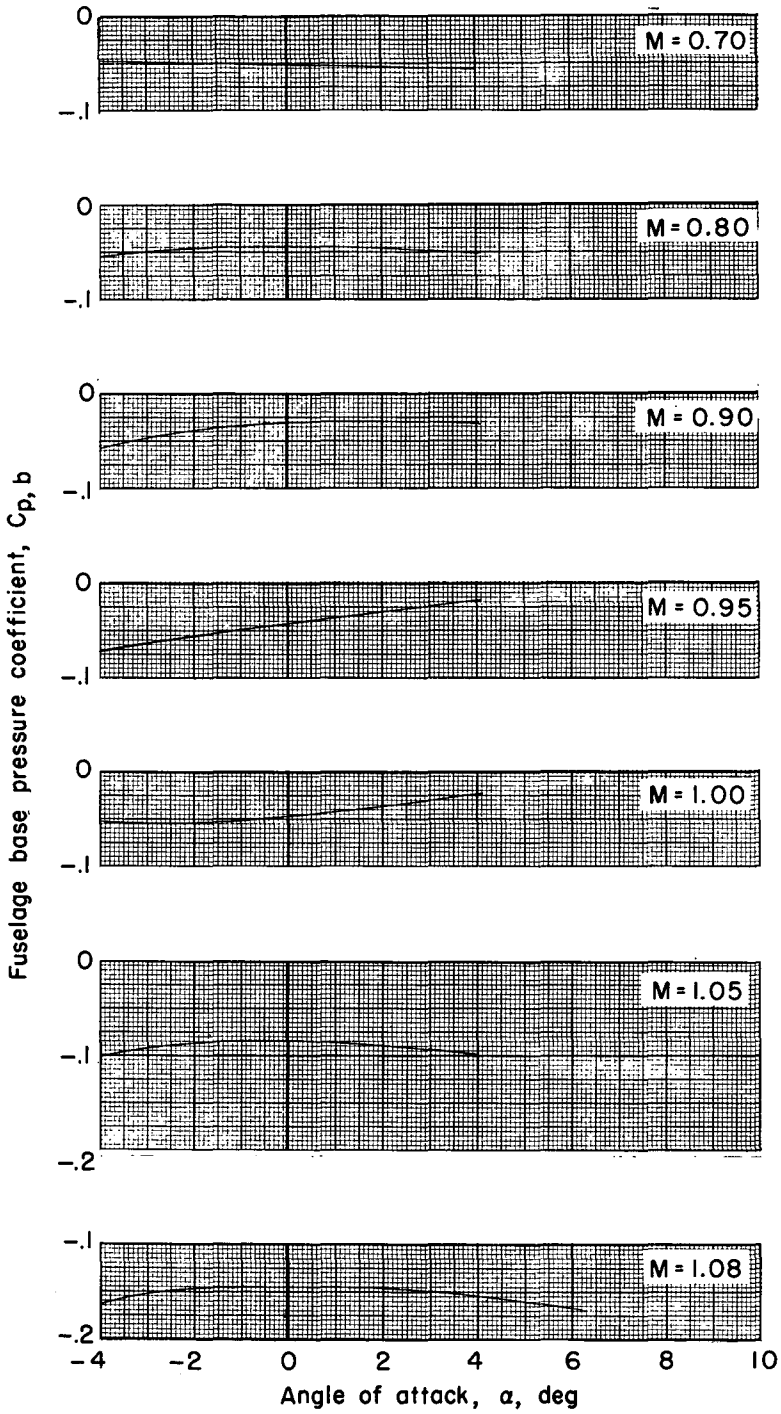

(c) Model 3.

Figure 14.- Concluded.

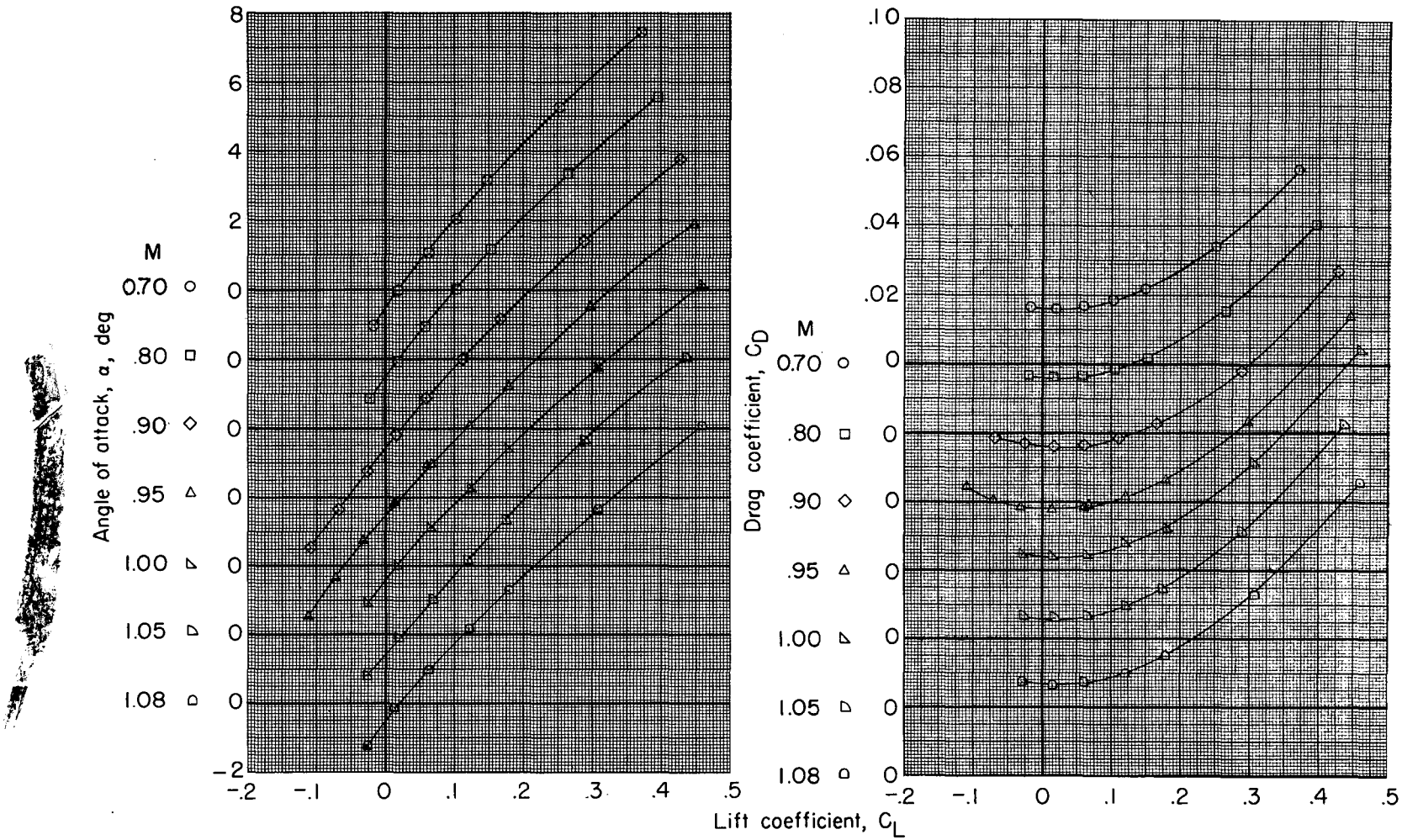

(a) Lift and drag coefficients.

Figure 15.- Aerodynamic characteristics for model 1.

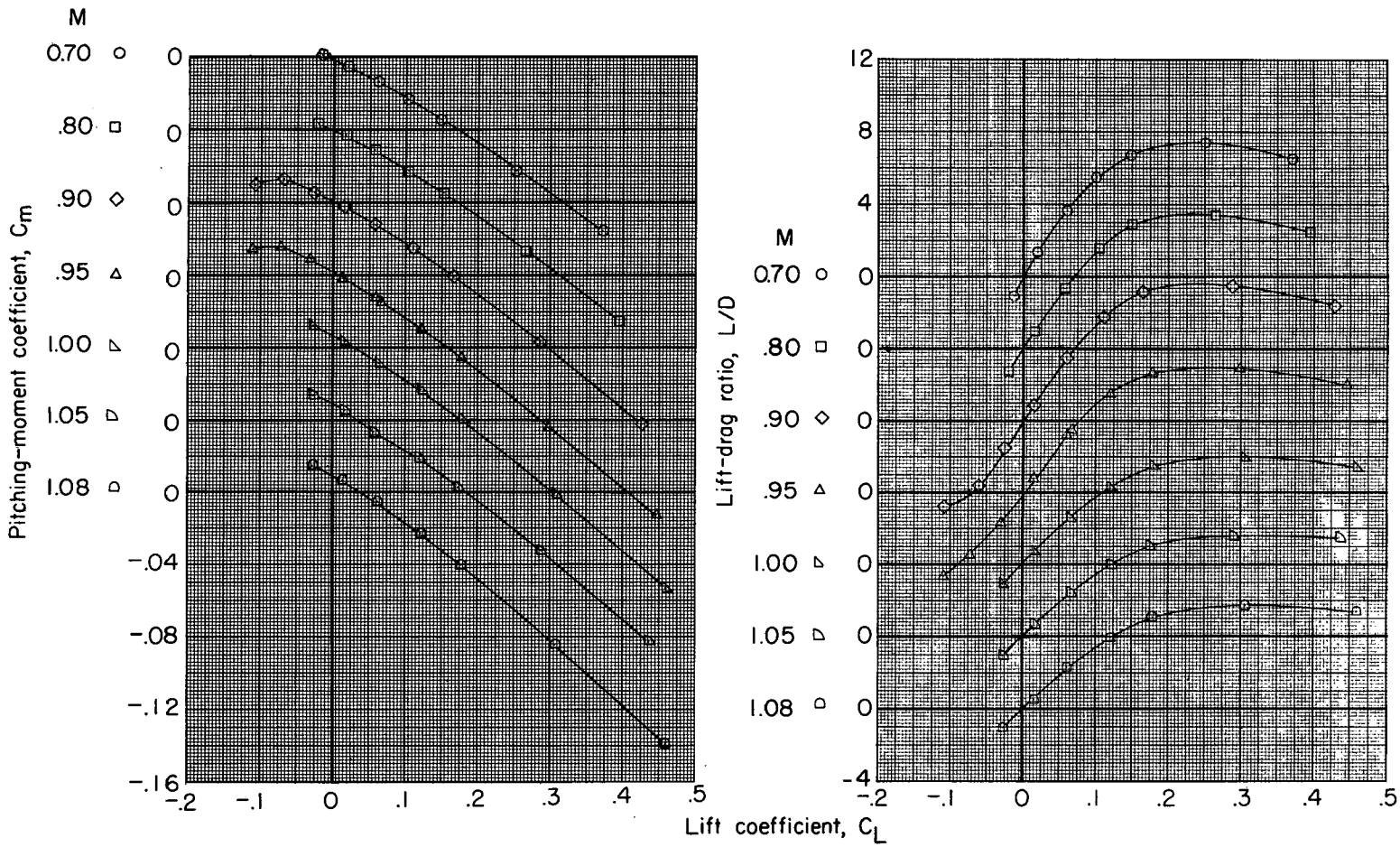

(b) Pitching-moment coefficients and lift-drag ratios.

Figure 15.- Concluded.

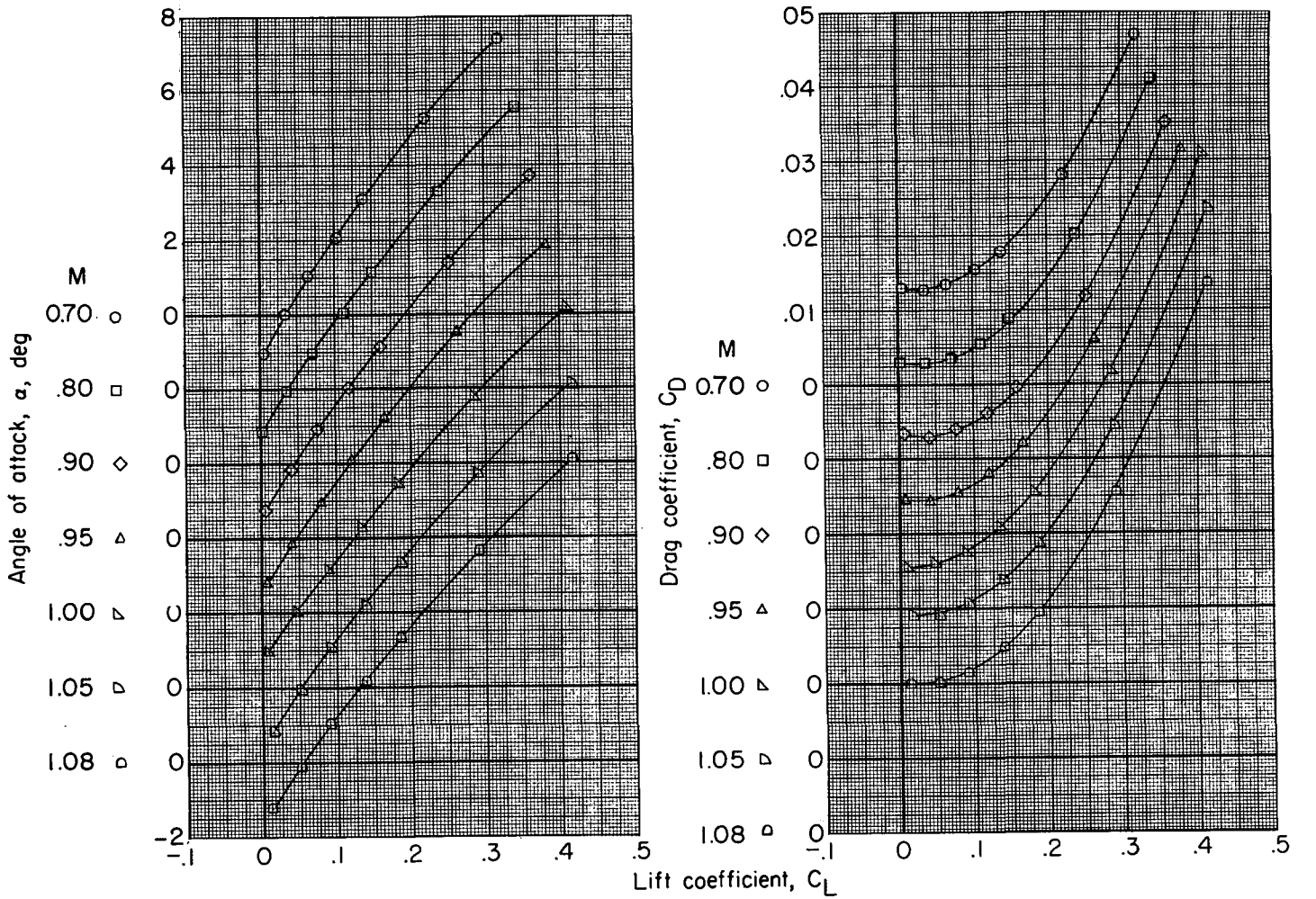

(a) Lift and drag coefficients.

Figure 16.- Aerodynamic characteristics for model 1 (tails off).

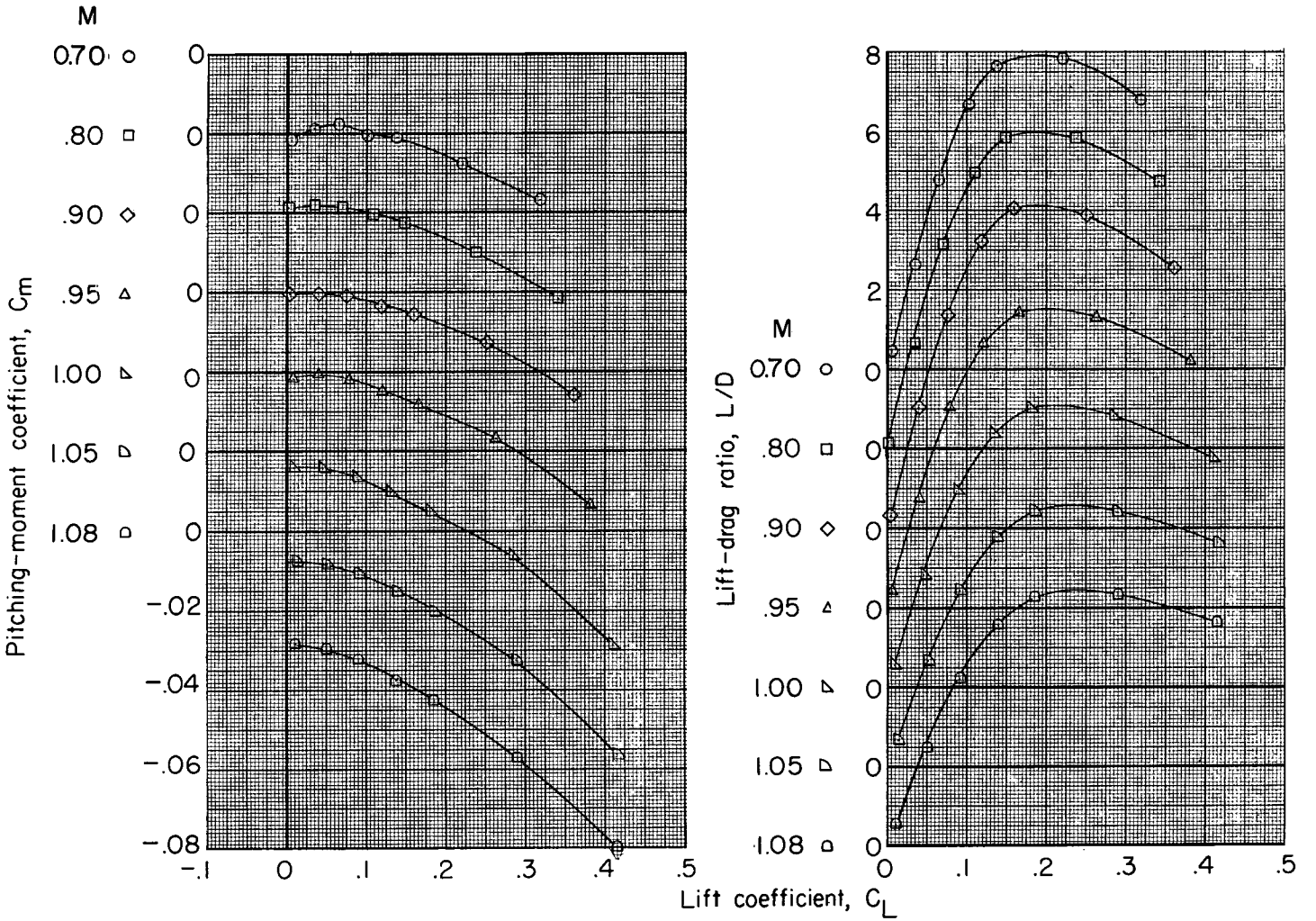

(b) Pitching-moment coefficients and lift-drag ratios.

Figure 16.- Concluded.

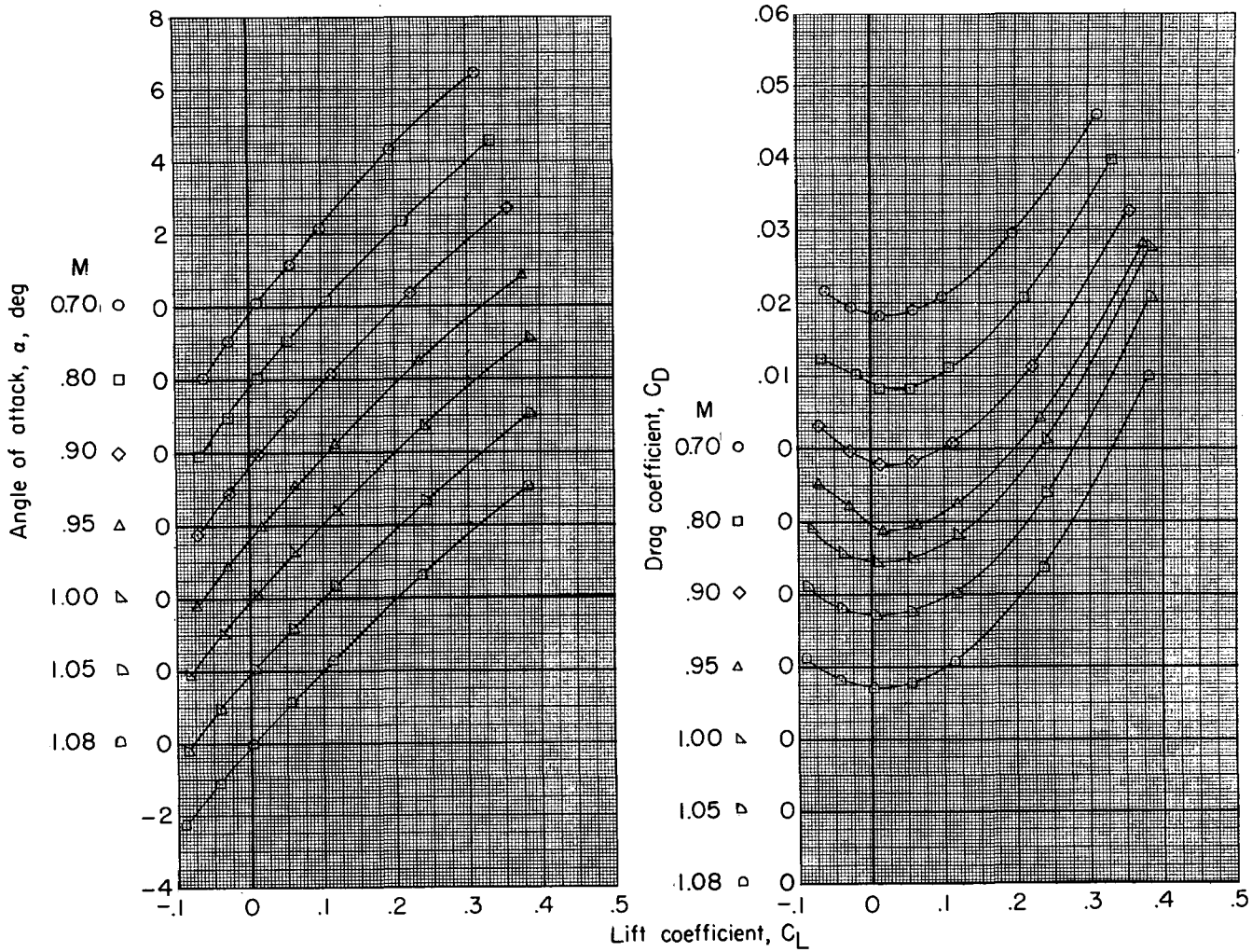

(a) Lift and drag coefficients.

Figure 17.- Aerodynamic characteristics for model 1A.

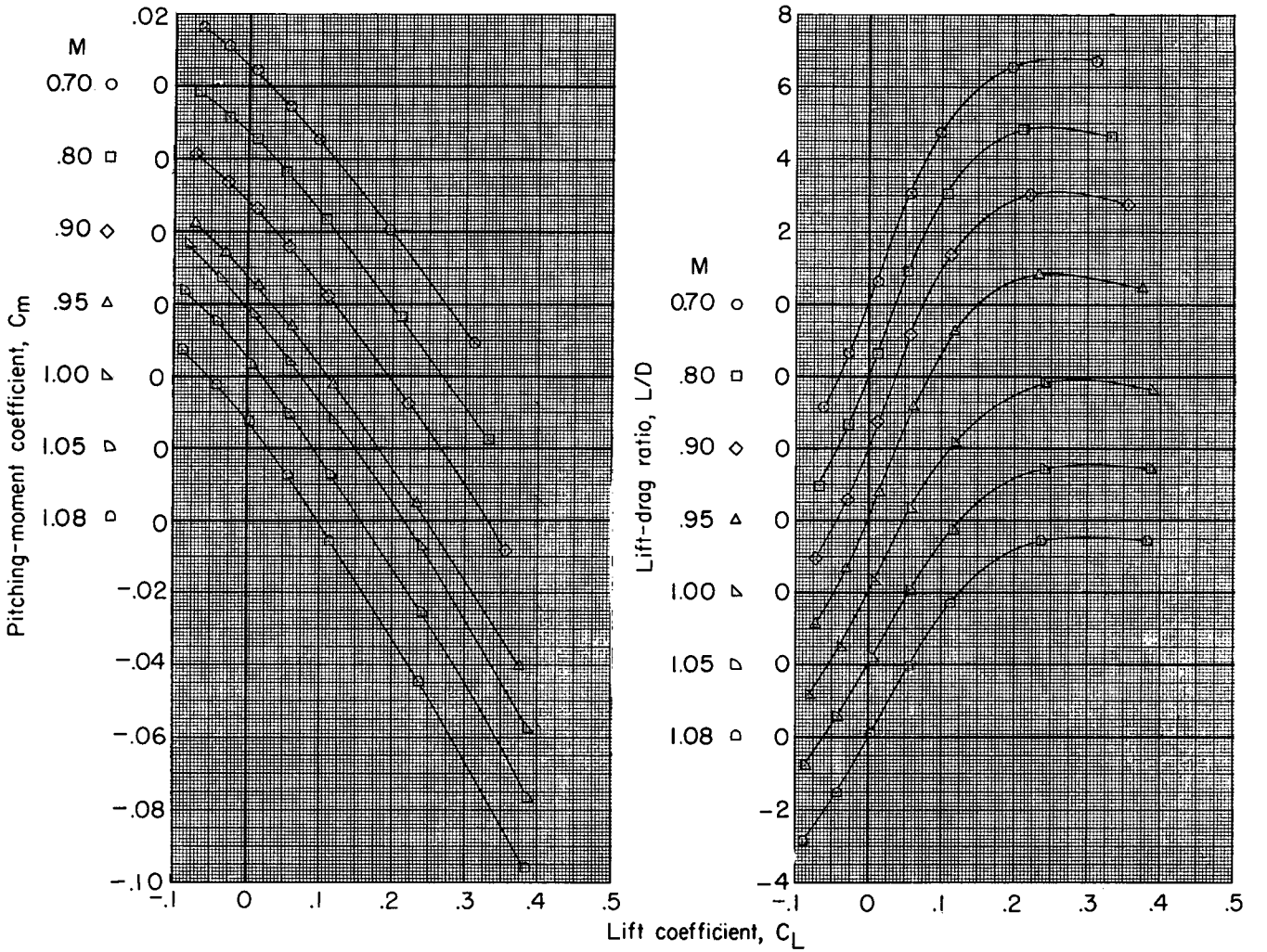

(b) Pitching-moment coefficients and lift-drag ratios.

Figure 17.- Concluded.

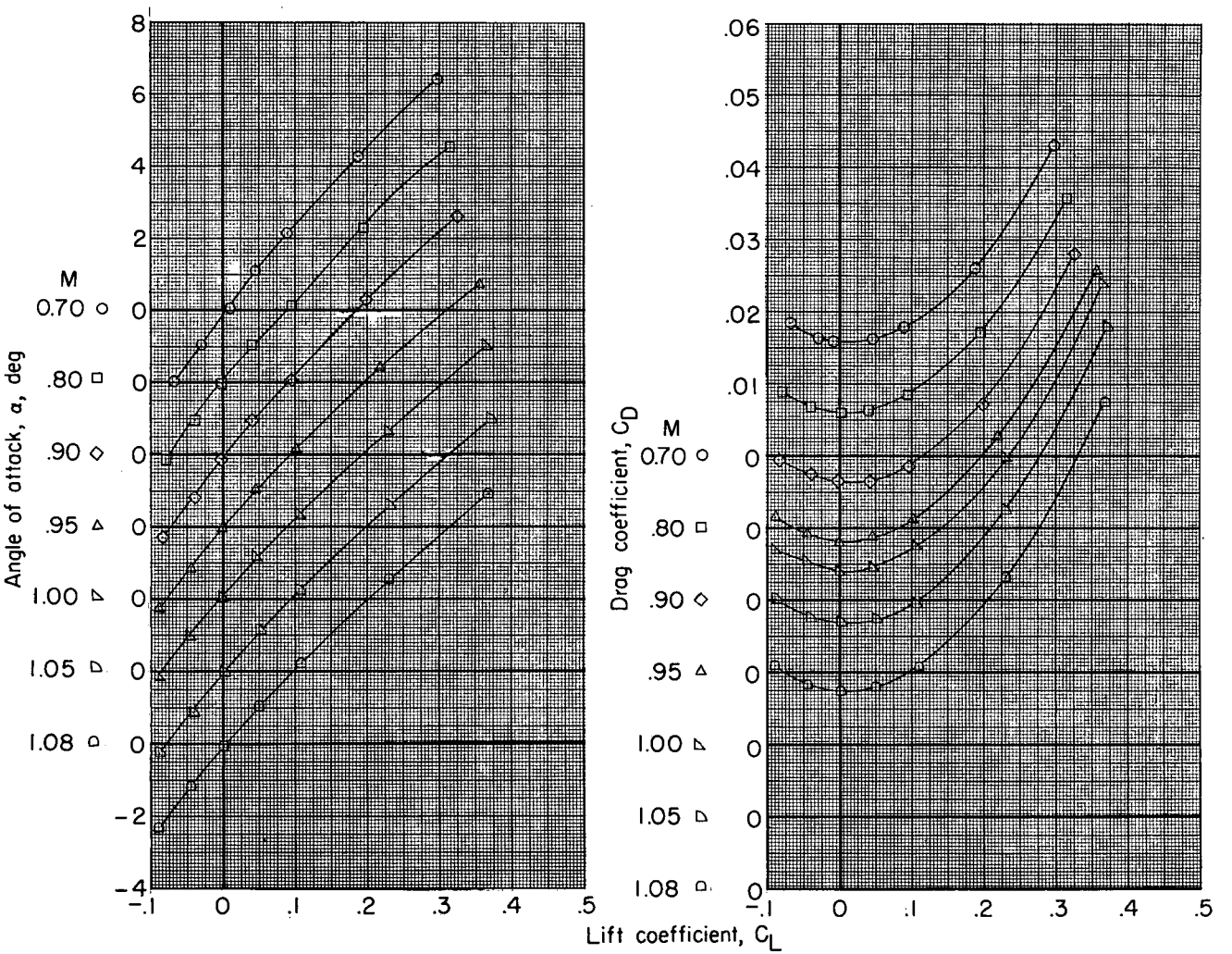

(a) Lift and drag coefficients.

Figure 18.- Aerodynamic characteristics for model 1B.

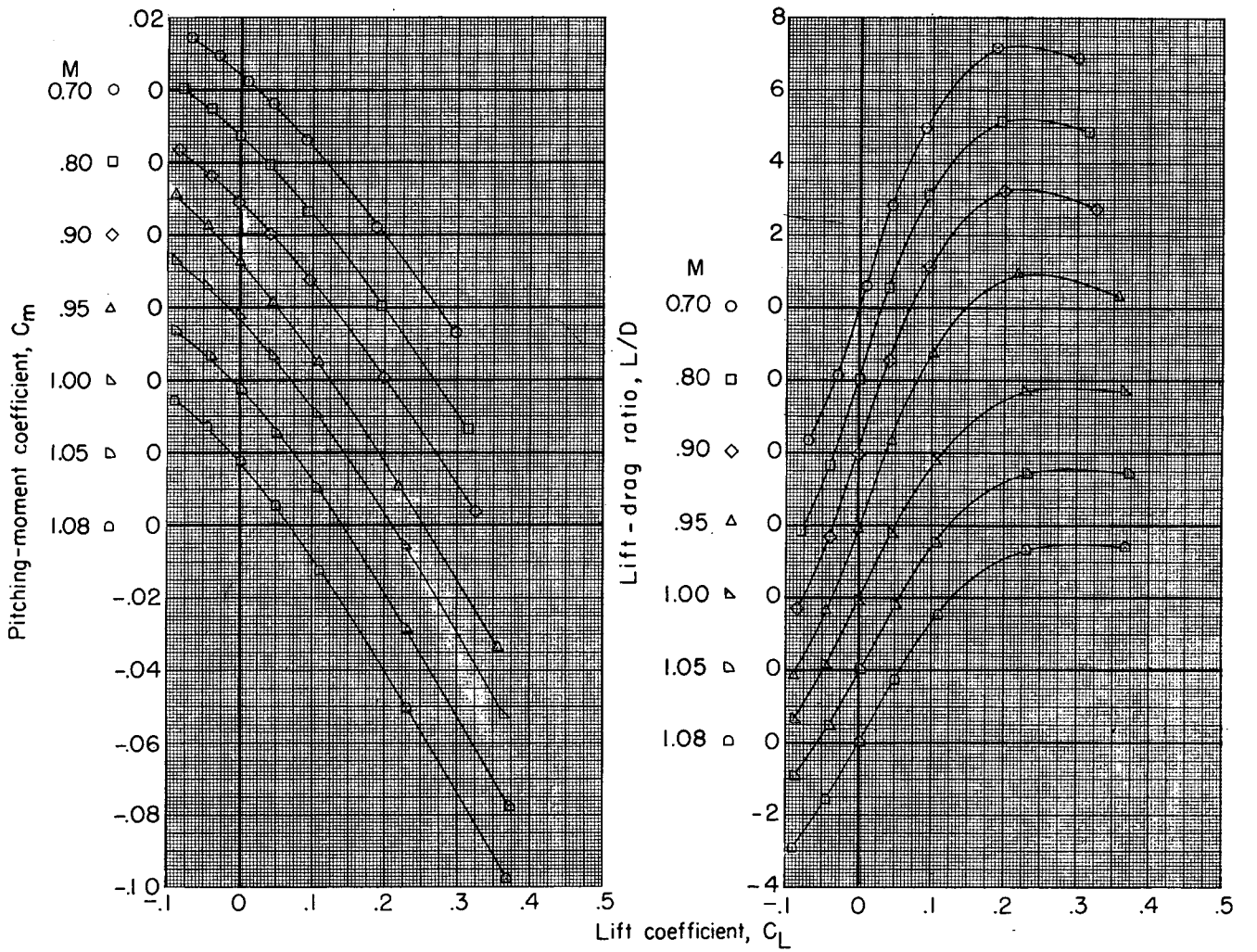

(b) Pitching-moment coefficients and lift-drag ratios.

Figure 18.- Concluded.

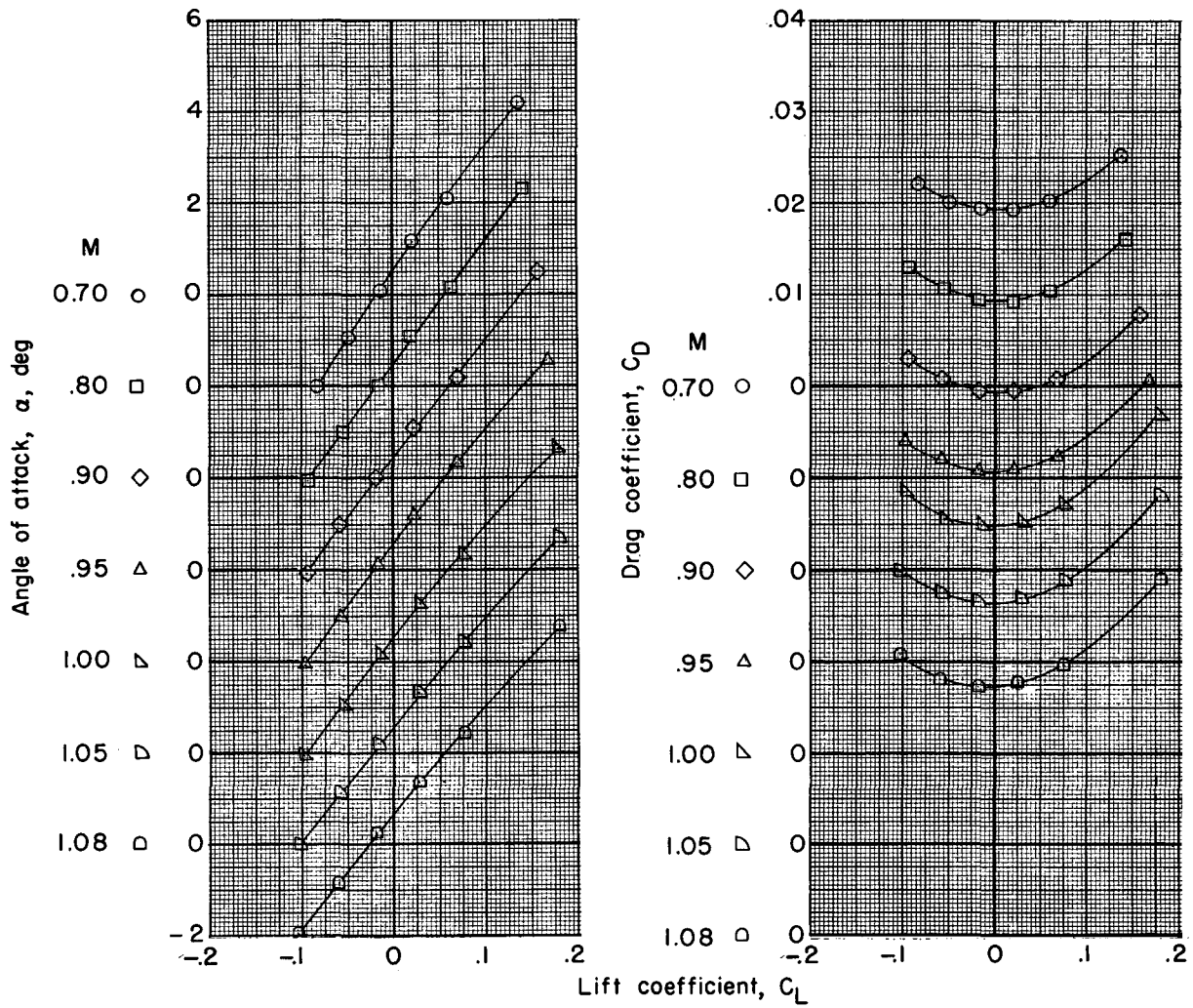

(a) Lift and drag coefficients.

Figure 19.- Aerodynamic characteristics for model 2.

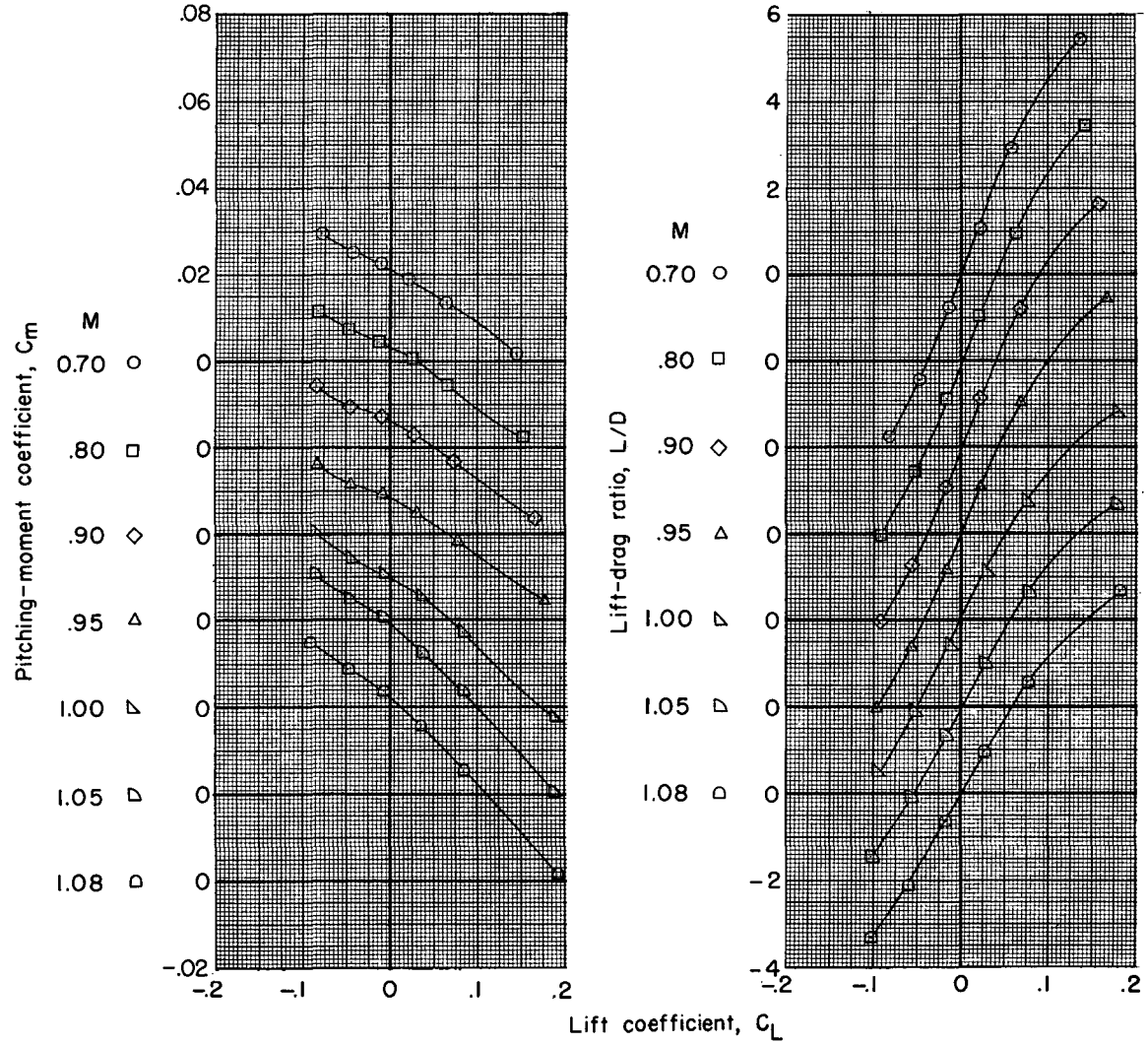

(b) Pitching-moment coefficients and lift-drag ratios.

Figure 19.- Concluded.

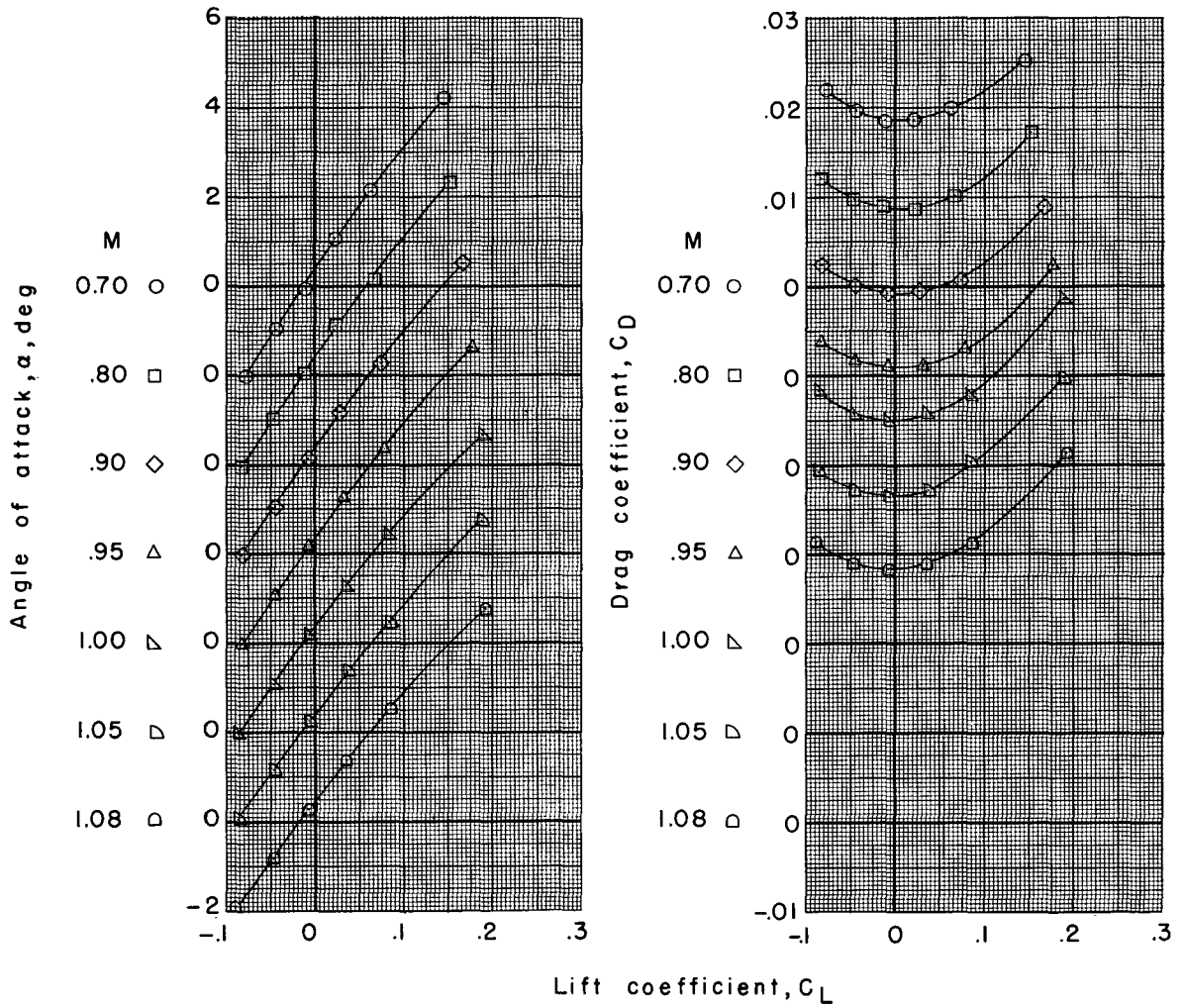

(a) Lift and drag coefficients.

Figure 20.- Aerodynamic characteristics for model 2A.

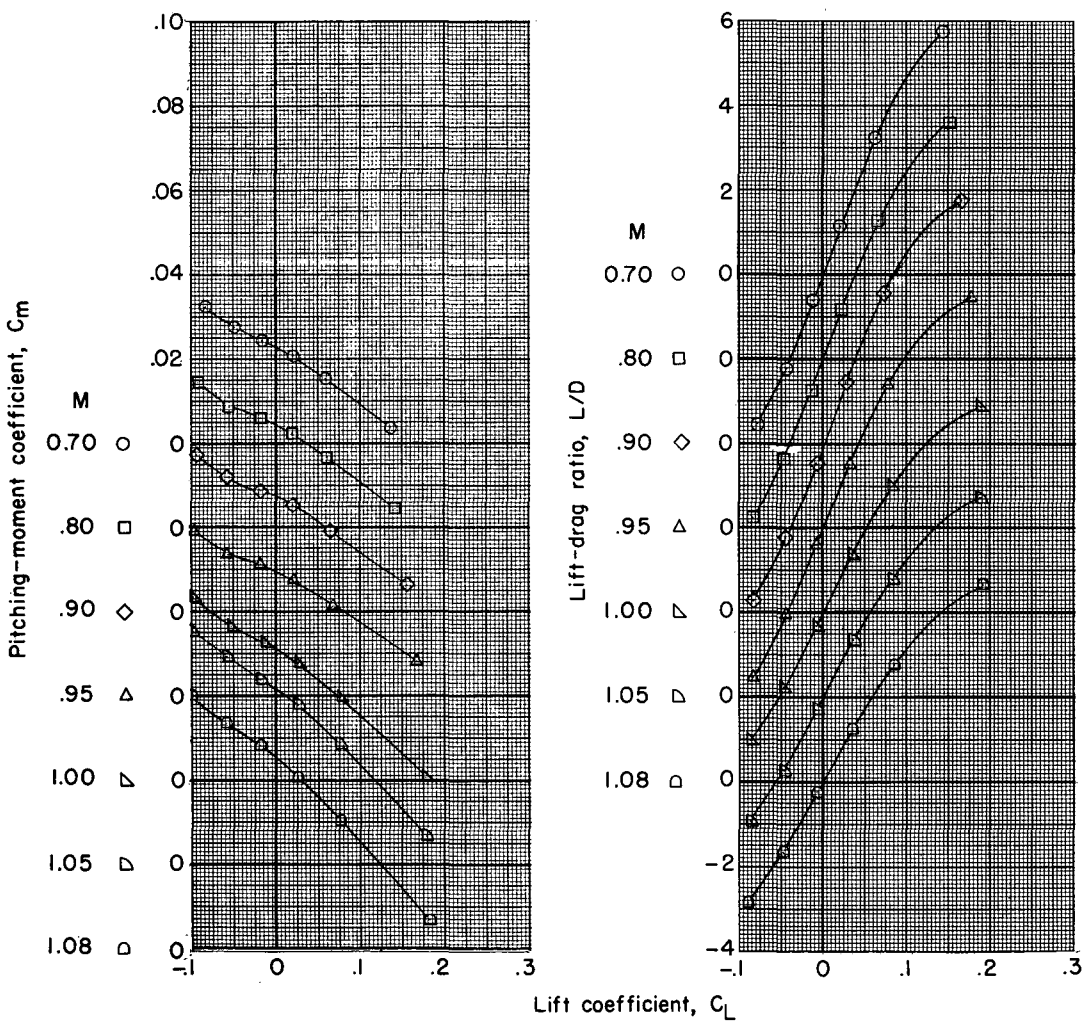

(b) Pitching-moment coefficient and lift-drag ratios.

Figure 20.- Concluded.

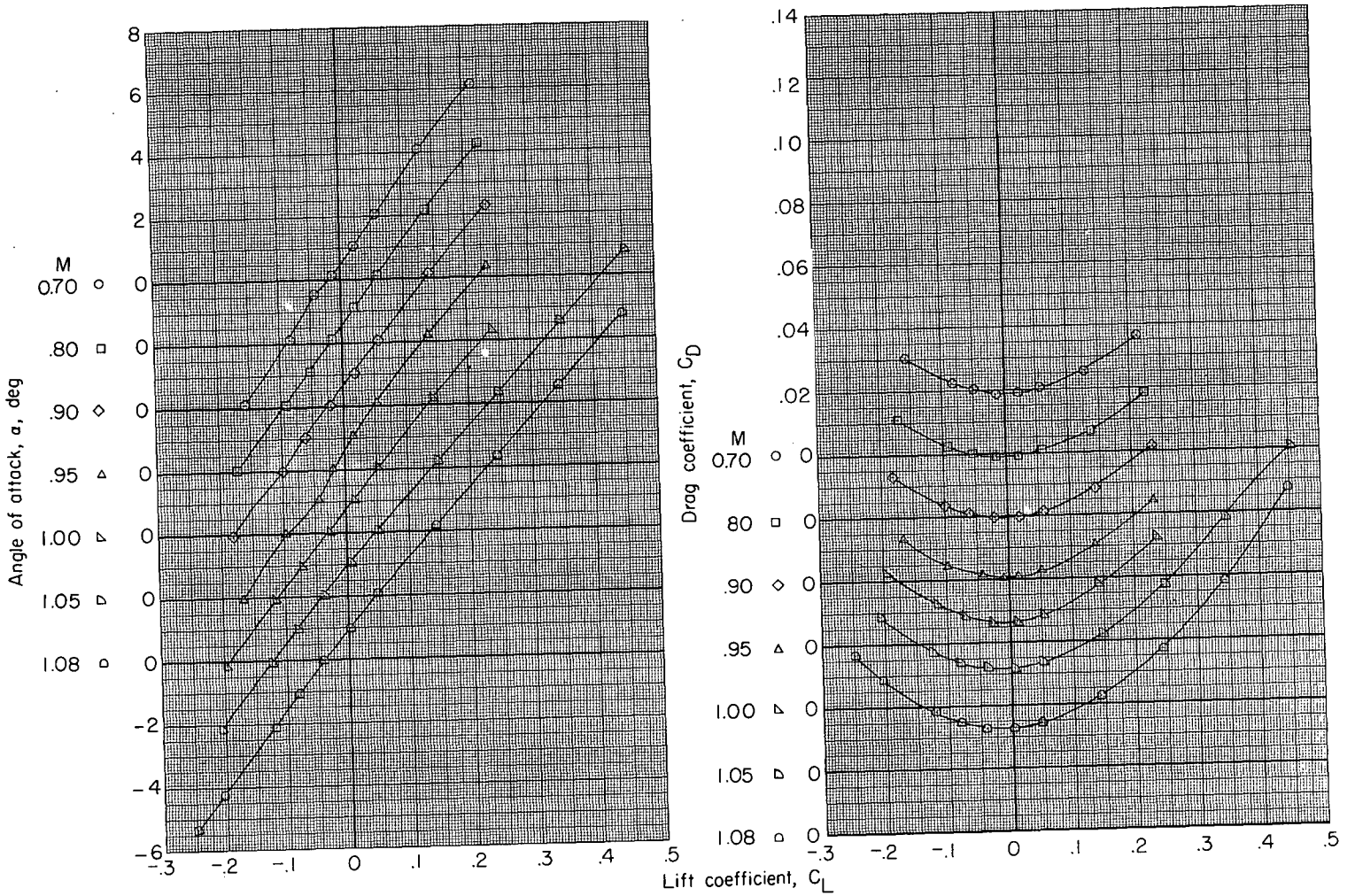

(a) Lift and drag coefficients.

Figure 21.- Aerodynamic characteristics for model 3.

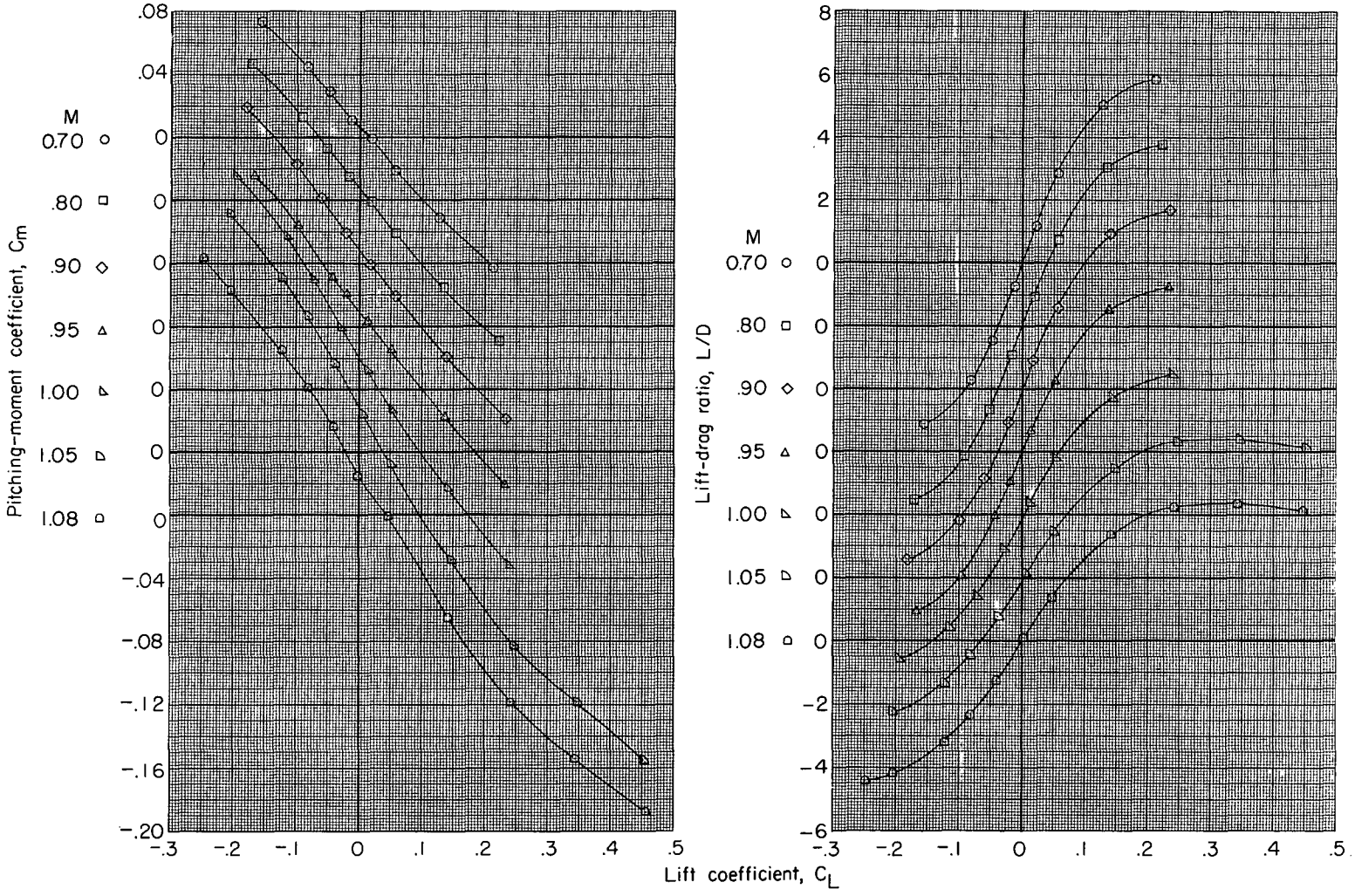

(b) Pitching-moment coefficients and lift-drag ratios.

Figure 21.- Concluded.

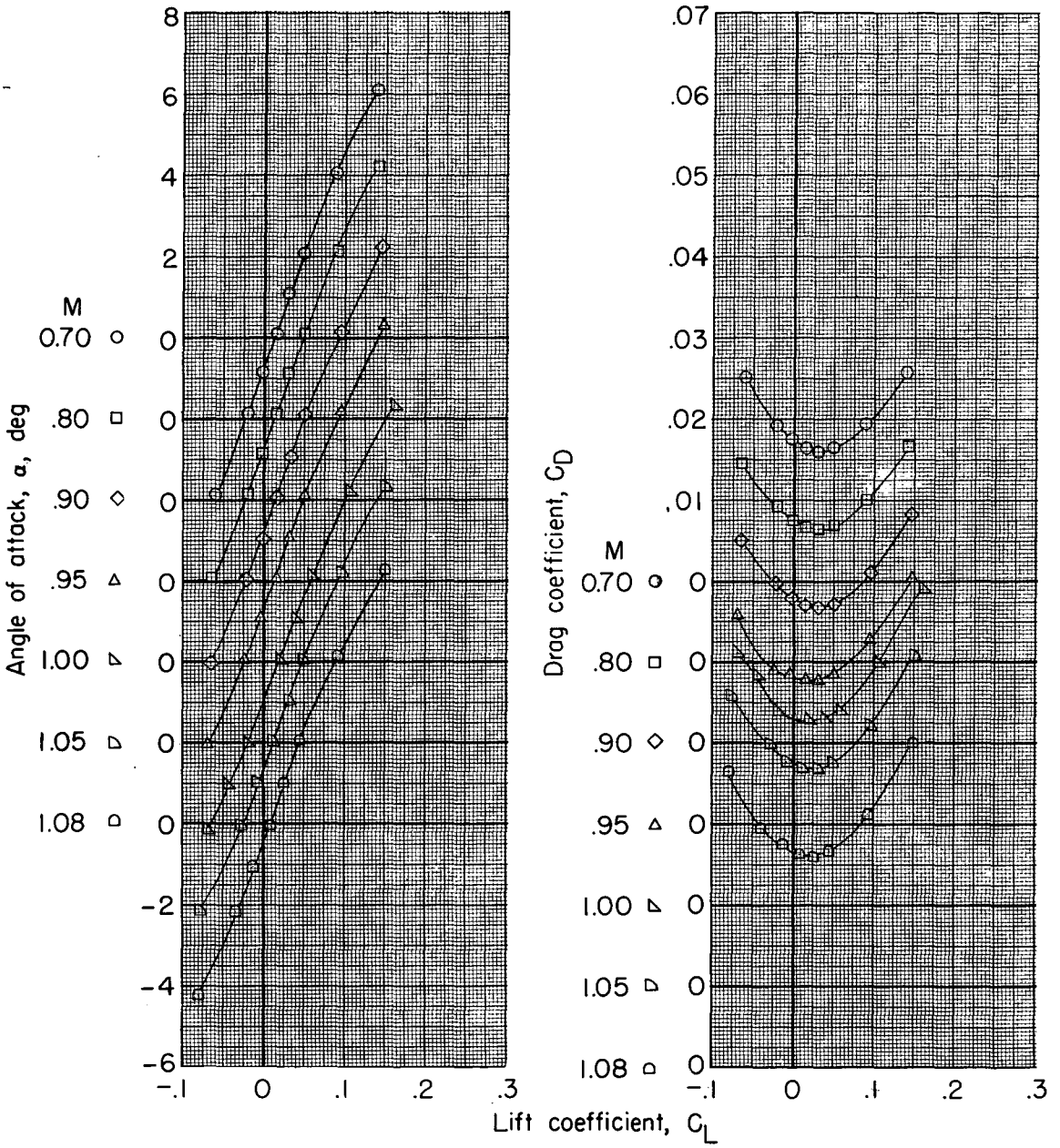

(a) Lift and drag coefficients.

Figure 22.- Aerodynamic characteristics for model 3 (tails off).

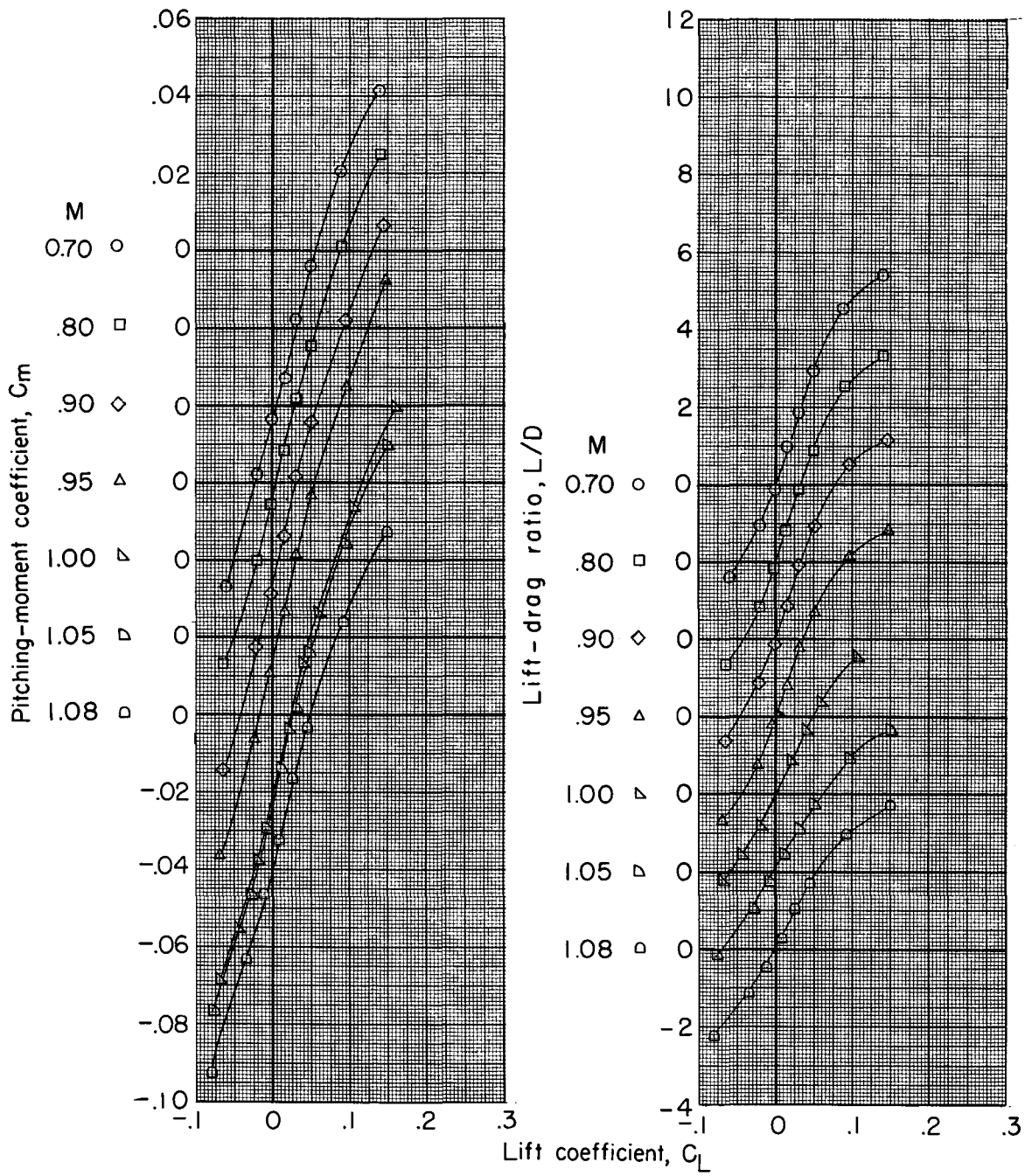

(b) Pitching-moment coefficients and lift-drag ratios.

Figure 22.- Concluded.

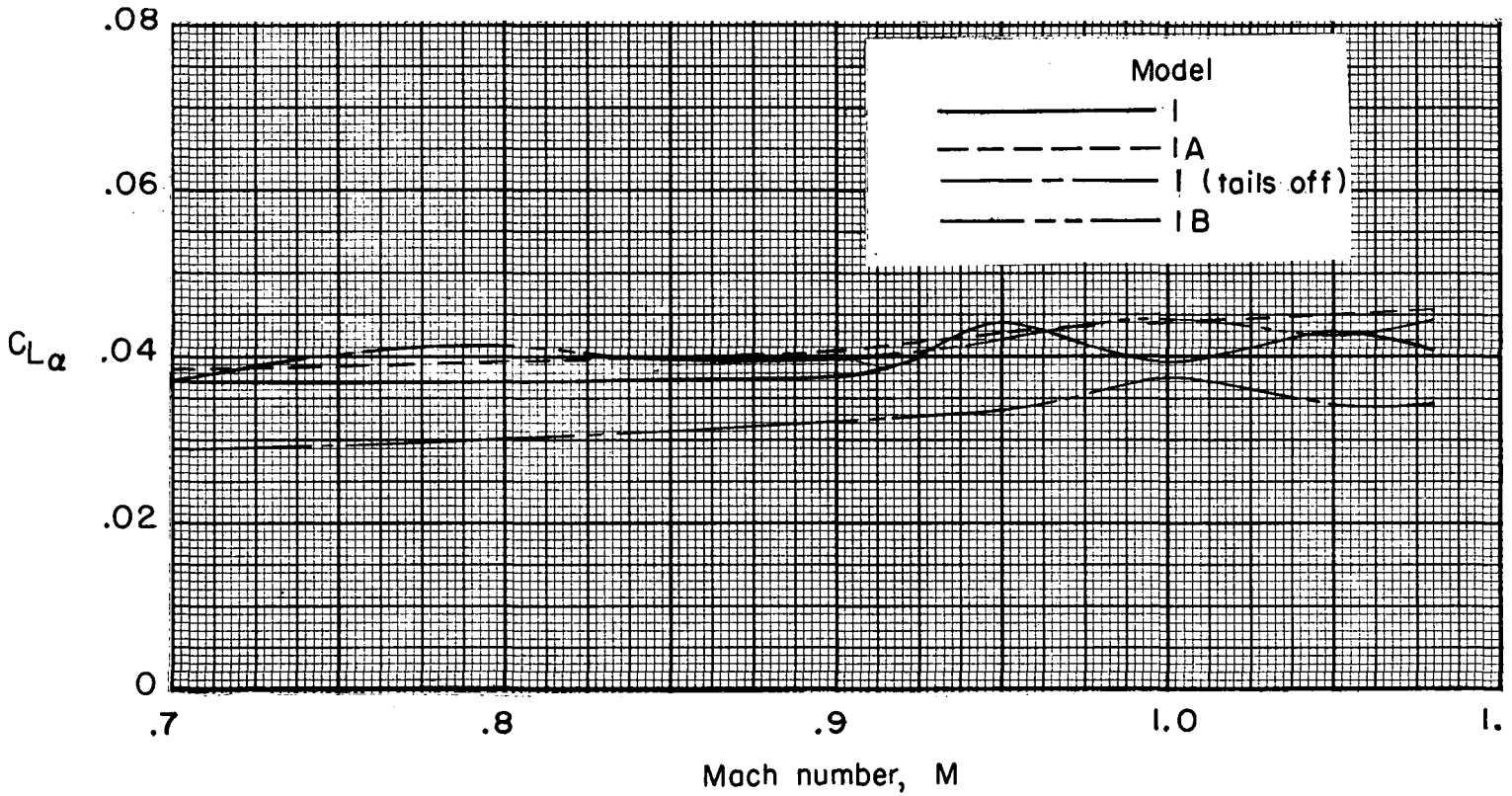

Figure 23.- Variation with Mach number of lift-curve slope for the various modifications to model 1.

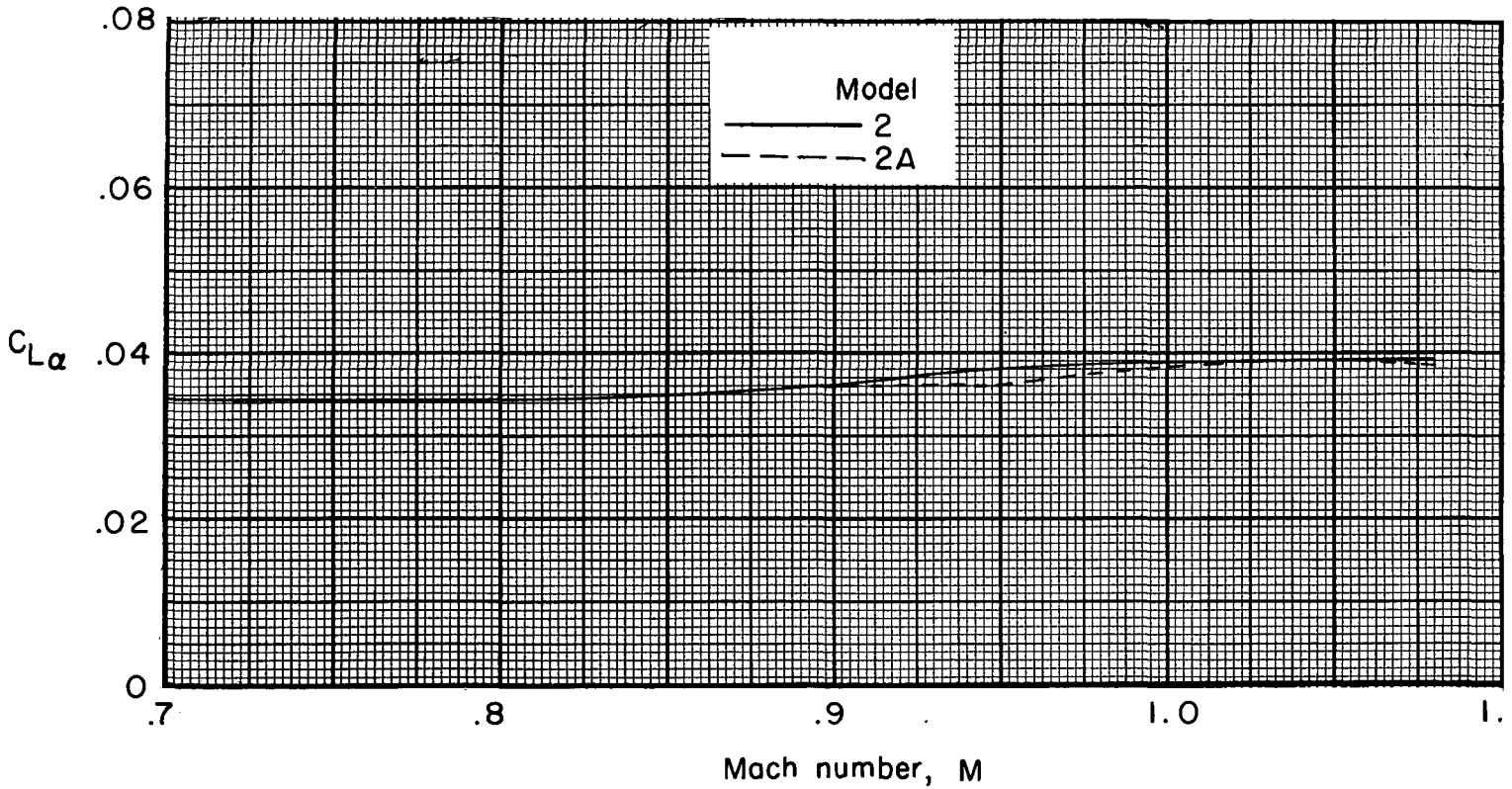

Figure 24.- Variation of lift-curve slope with Mach number for models 2 and 2A.

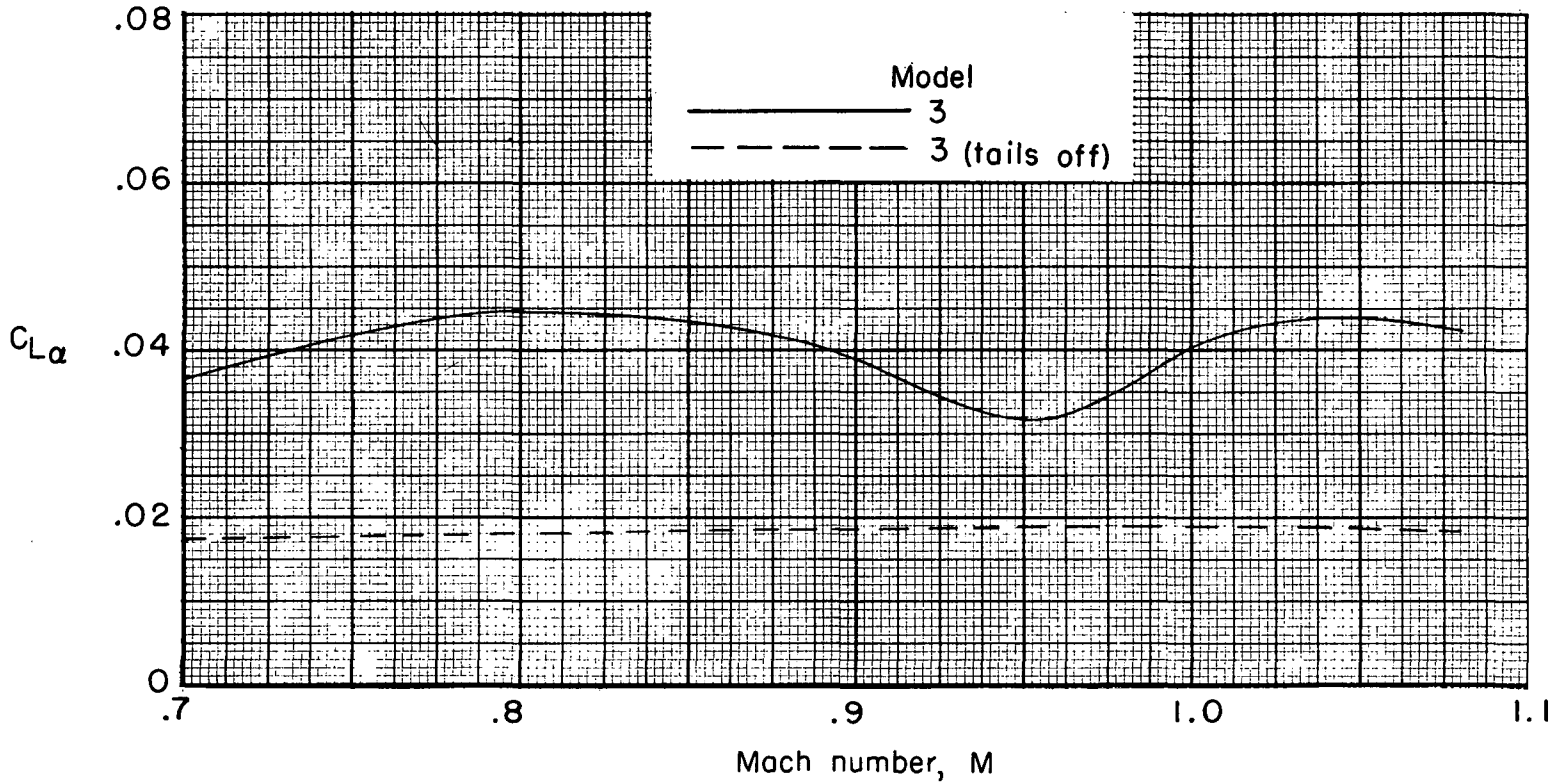

Figure 25.- Variation of lift-curve slope with Mach number for model 3.

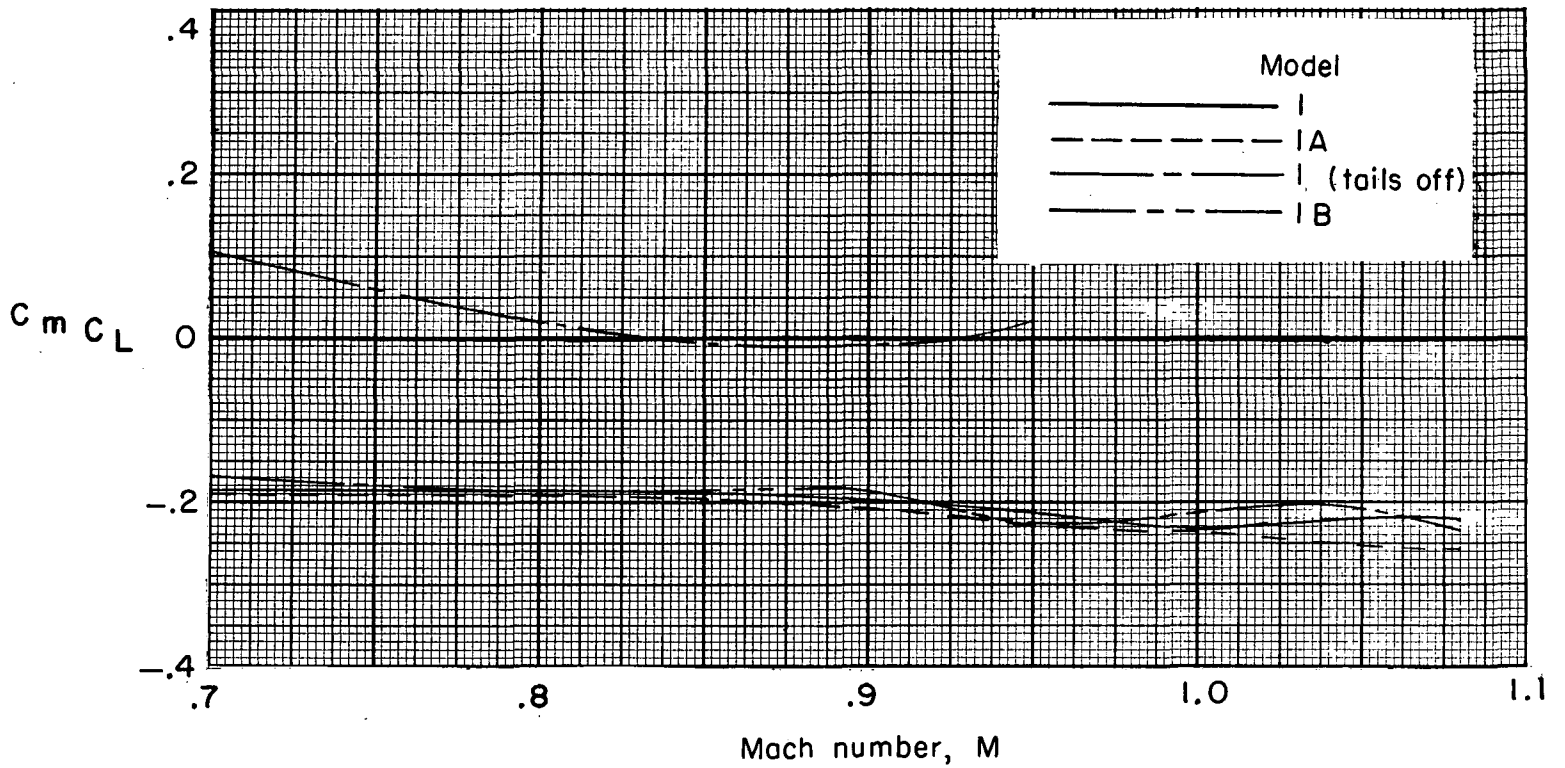

(a) $C_L = 0$.

Figure 26.- Variation with Mach number of pitching-moment-curve slope at $C_L = 0$ and 0.025 for the various modifications to model 1.

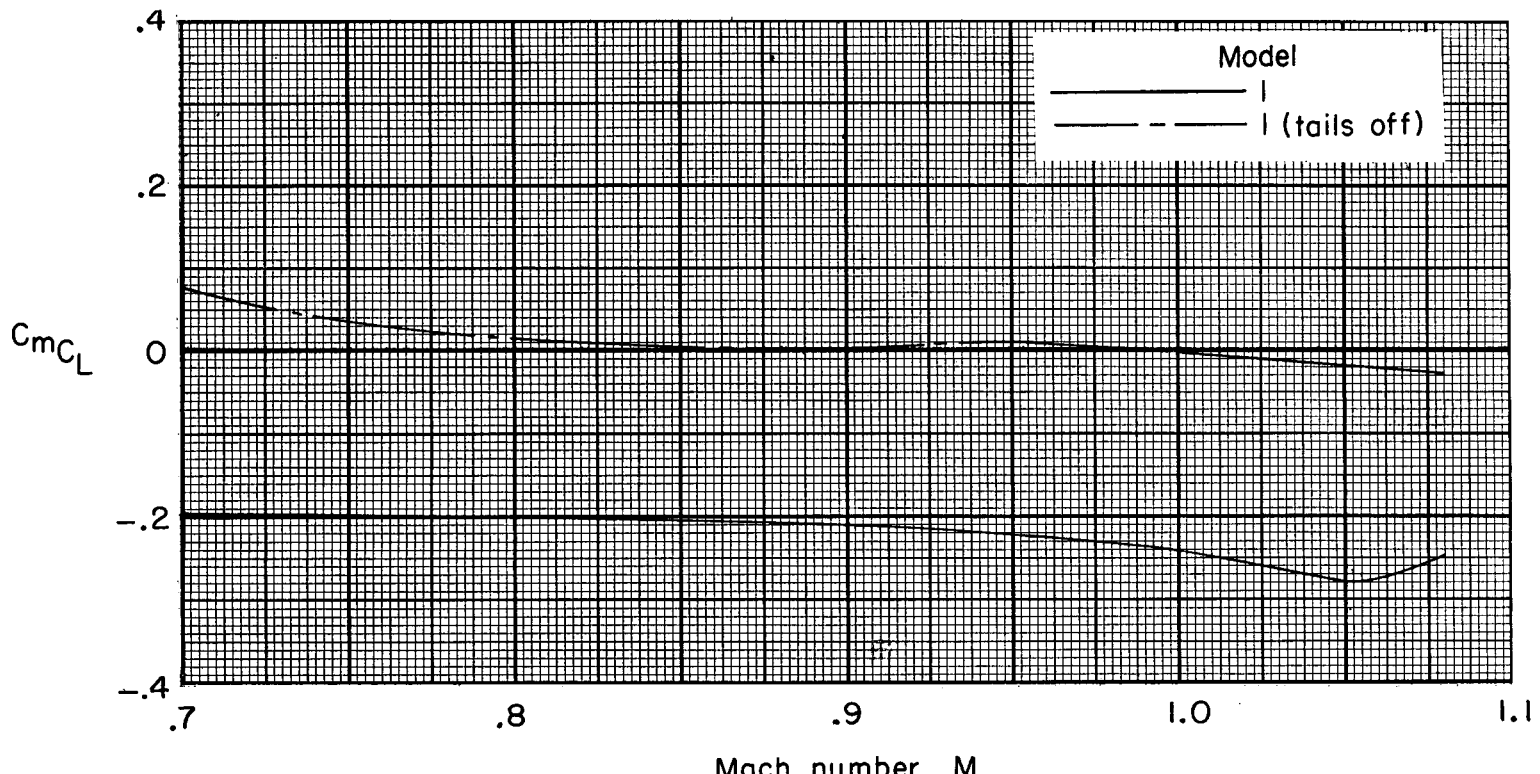

(b) $C_L = 0.025$.

Figure 26.- Concluded.

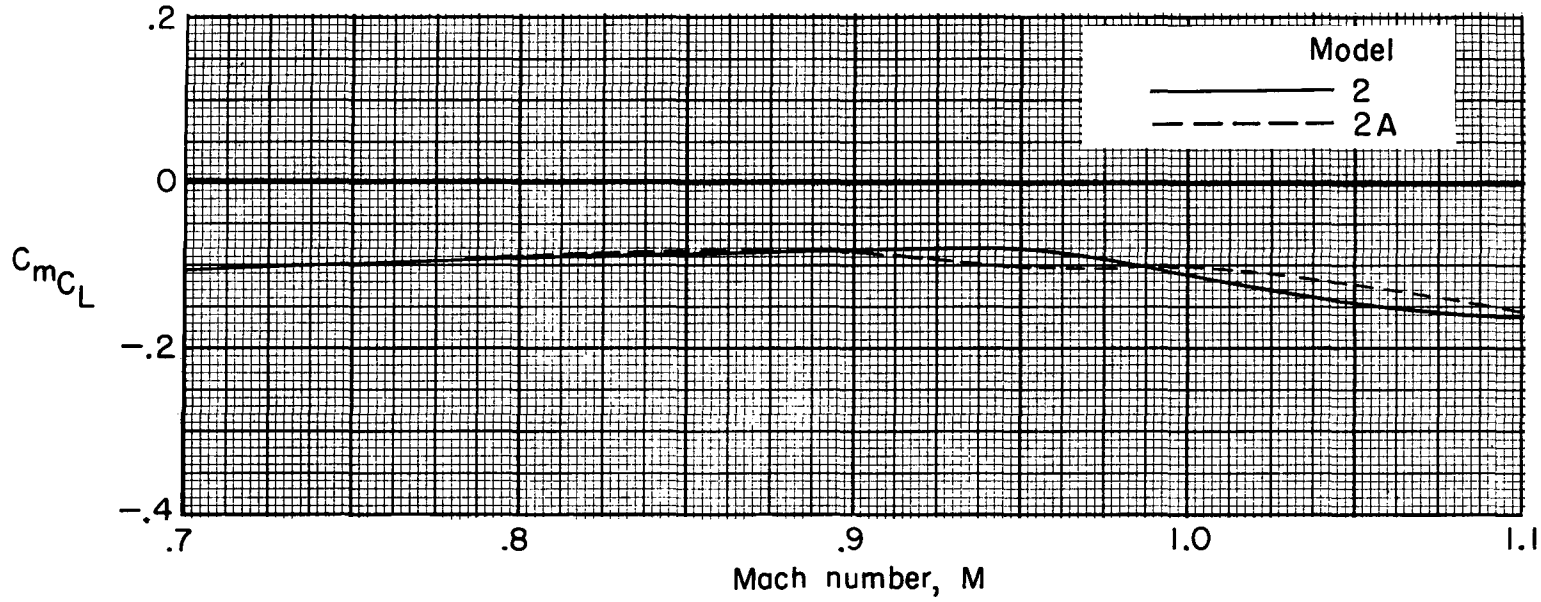

Figure 27.- Variation of pitching-moment-curve slope with Mach number for models 2 and 2A.

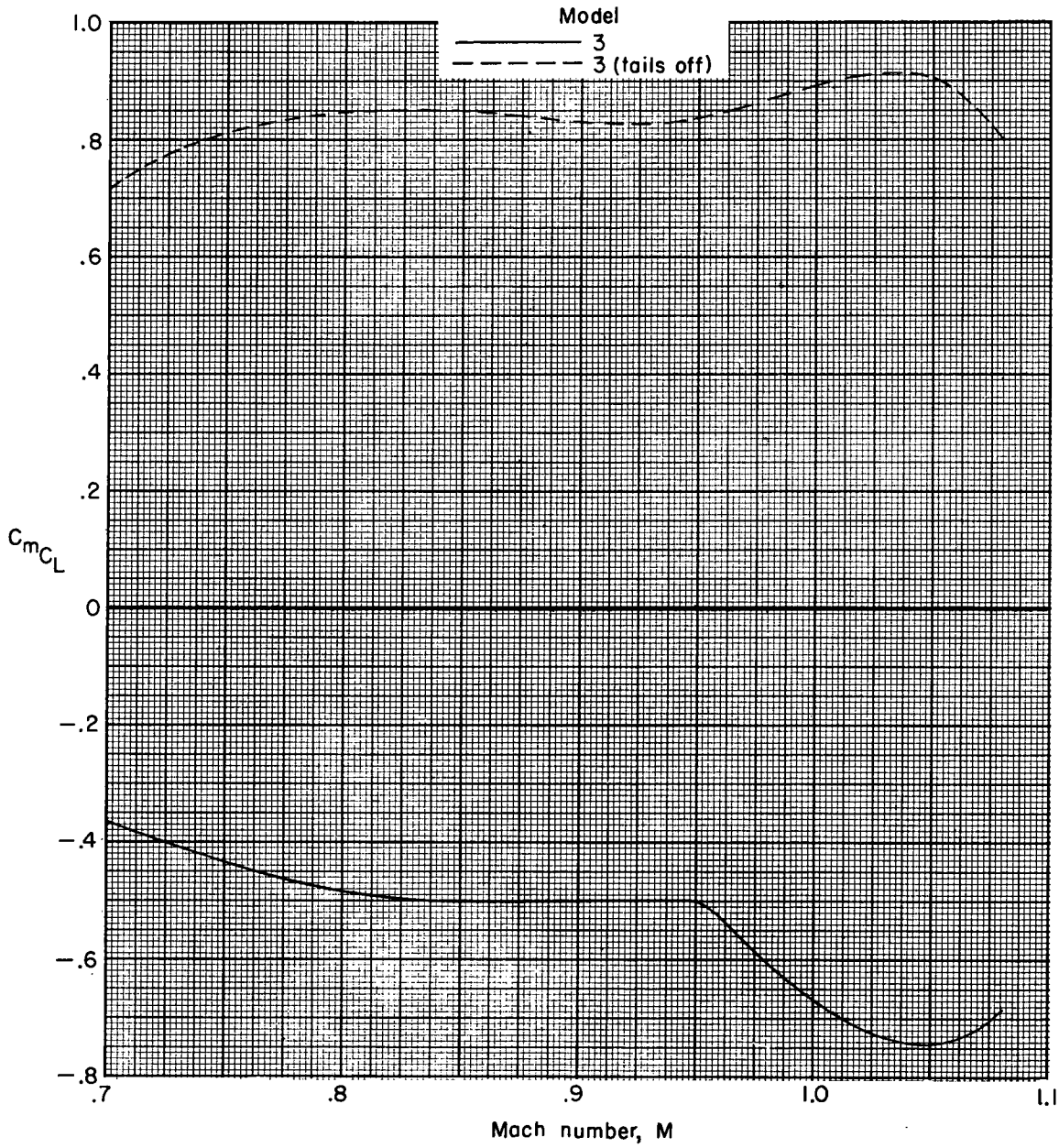

Figure 28.- Variation of pitching-moment-curve slope with Mach number for model 3.

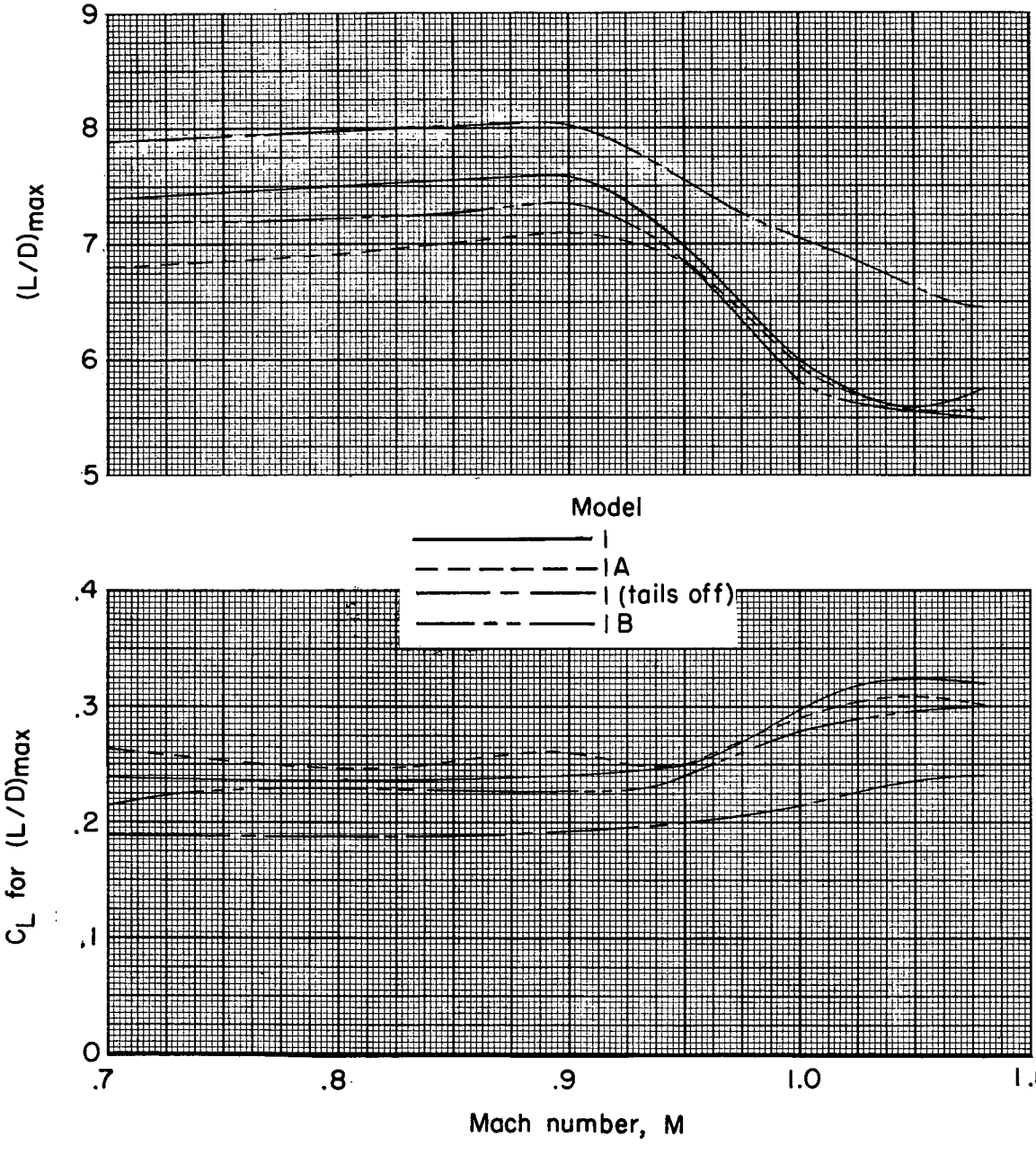

Figure 29.- Variation with Mach number of maximum lift-drag ratios and lift coefficient for $(L/D)_{max}$ for the various modifications to model 1.

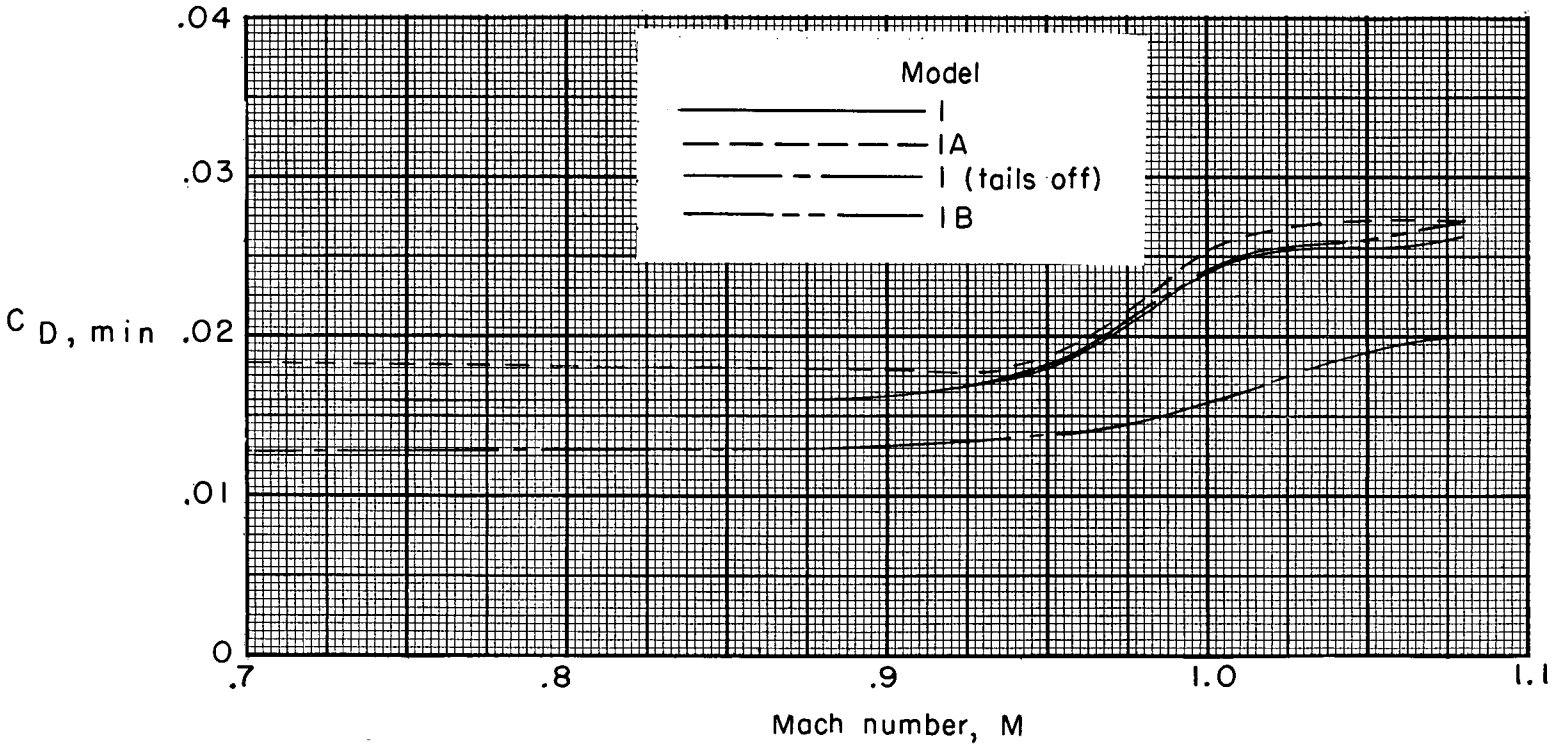

Figure 30.- A comparison of the minimum drag characteristics for the various modifications to model 1.

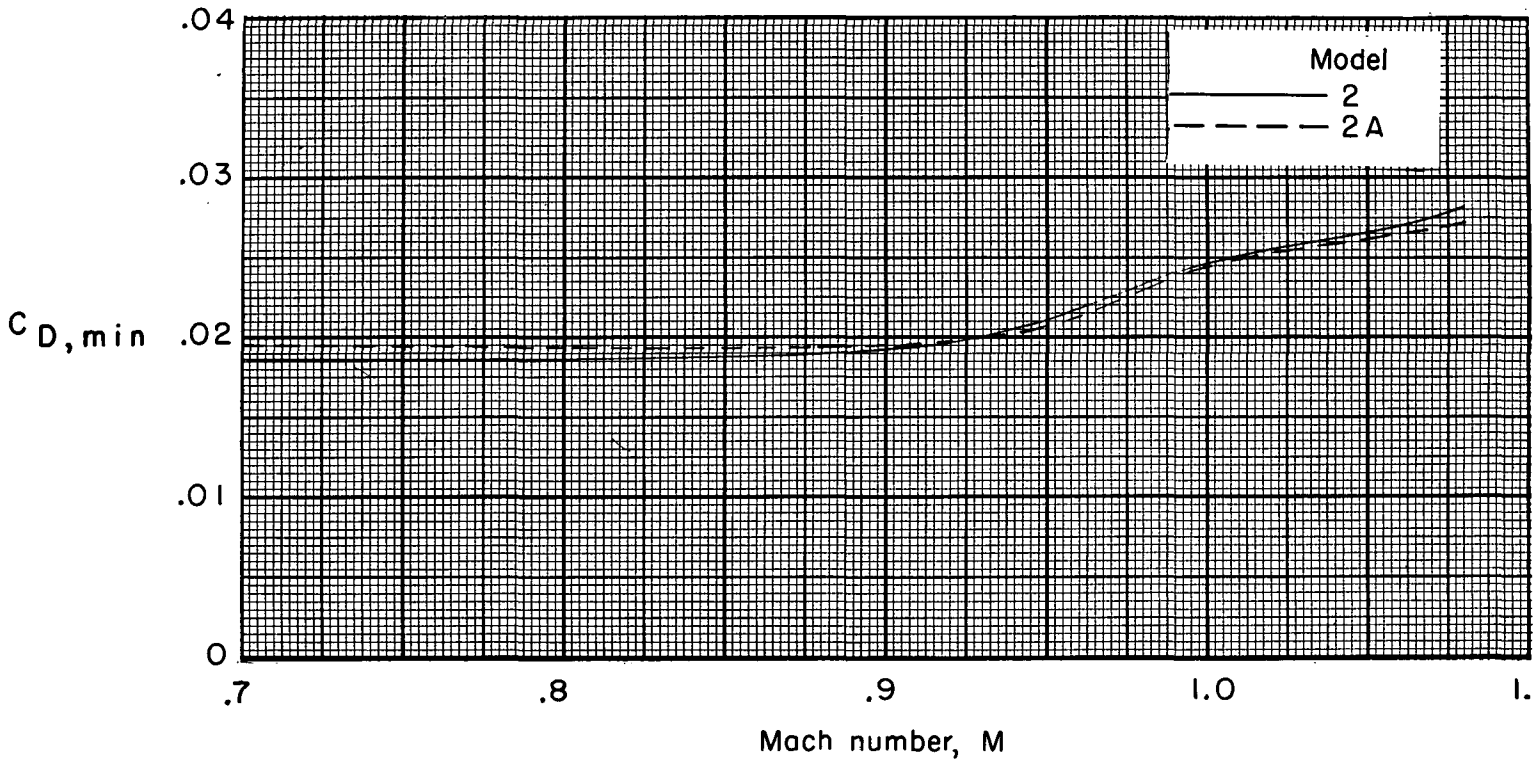

Figure 31.- A comparison of the minimum drag characteristics for models 2 and 2A.

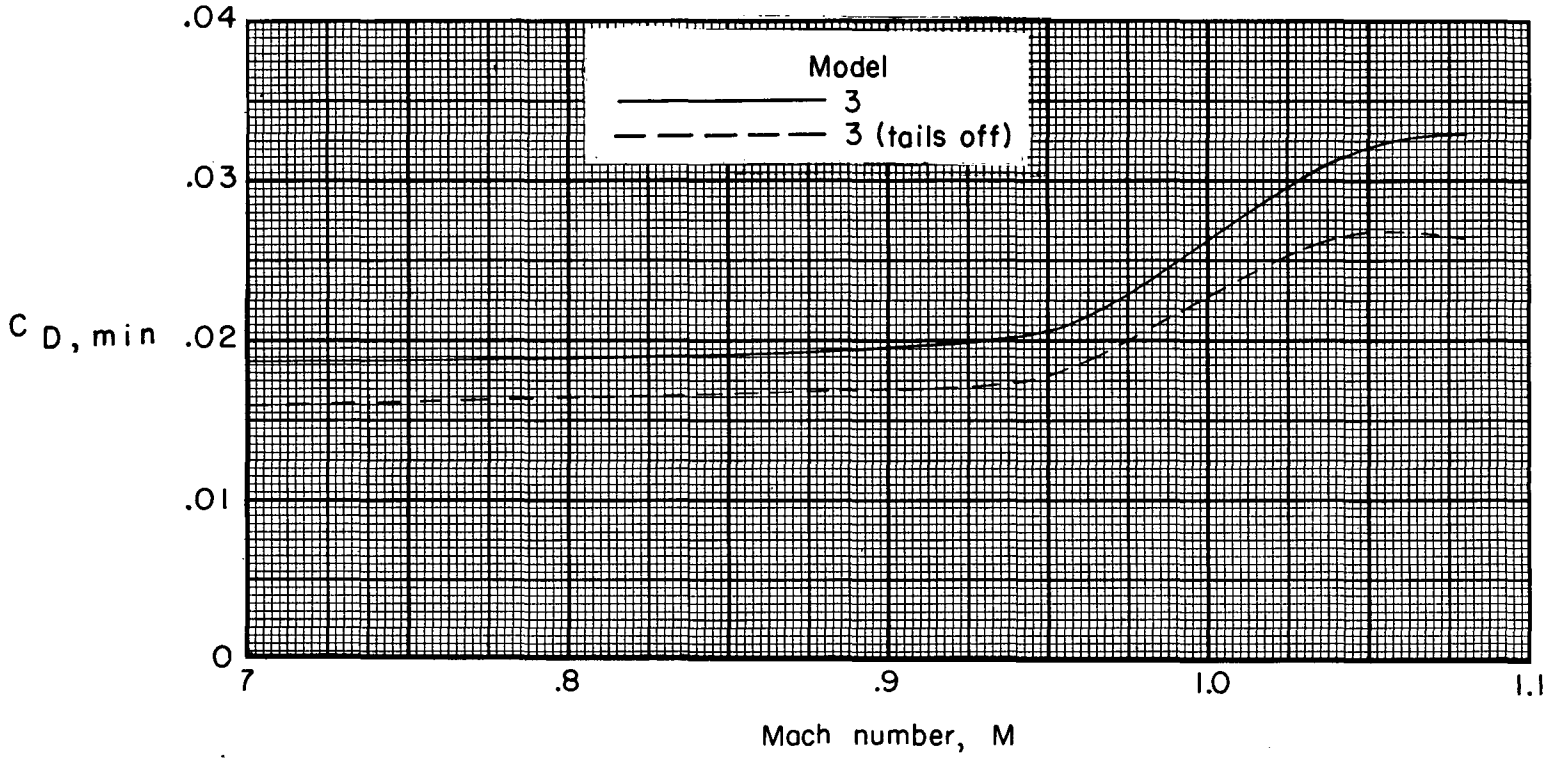

Figure 32.- A comparison of the minimum drag characteristics for model 3.

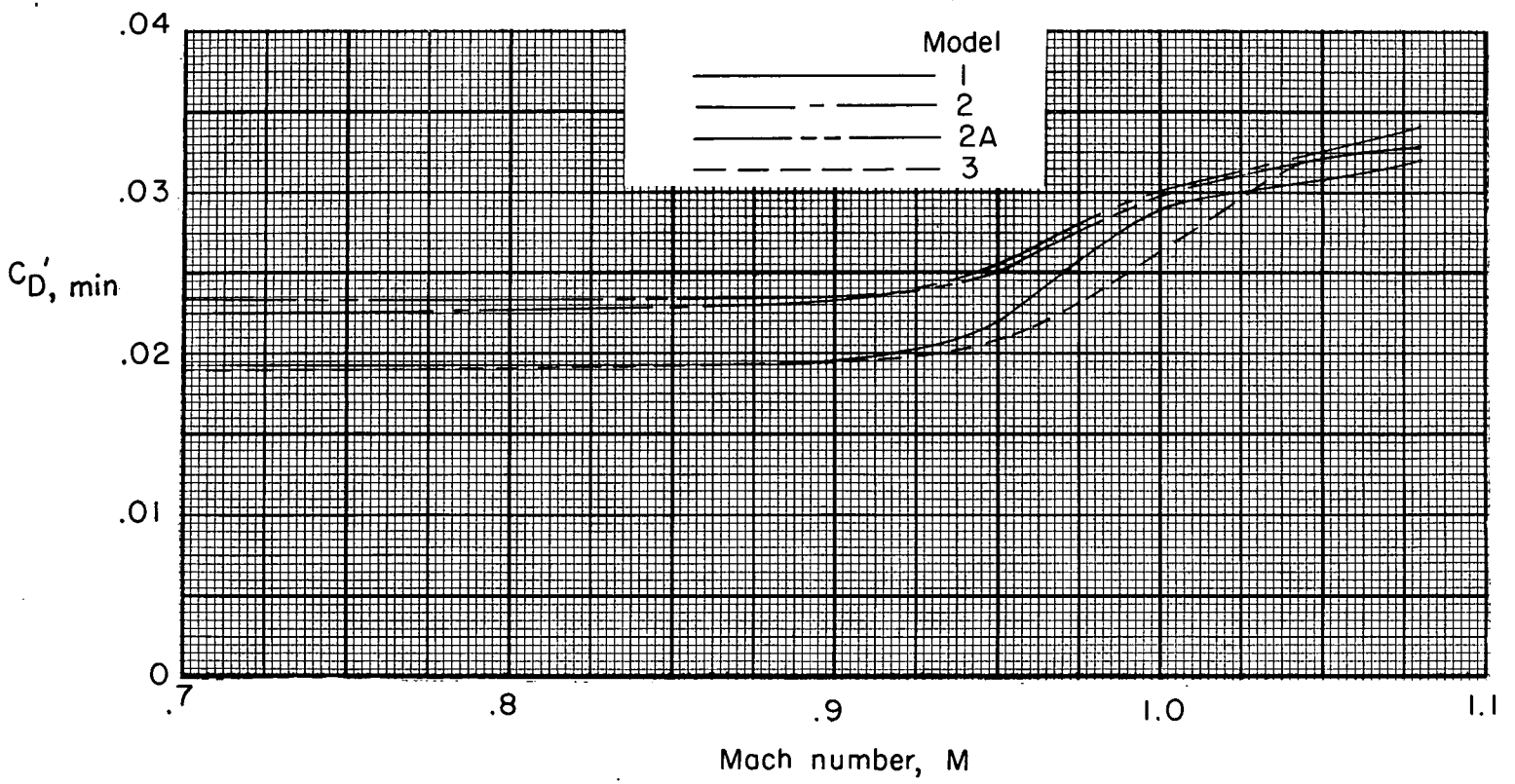

Figure 33.- A comparison of the minimum drag characteristics for models 1, 2, 2A, and 3.

NASA-Langley, 1962 L-3043

L-3043